Article

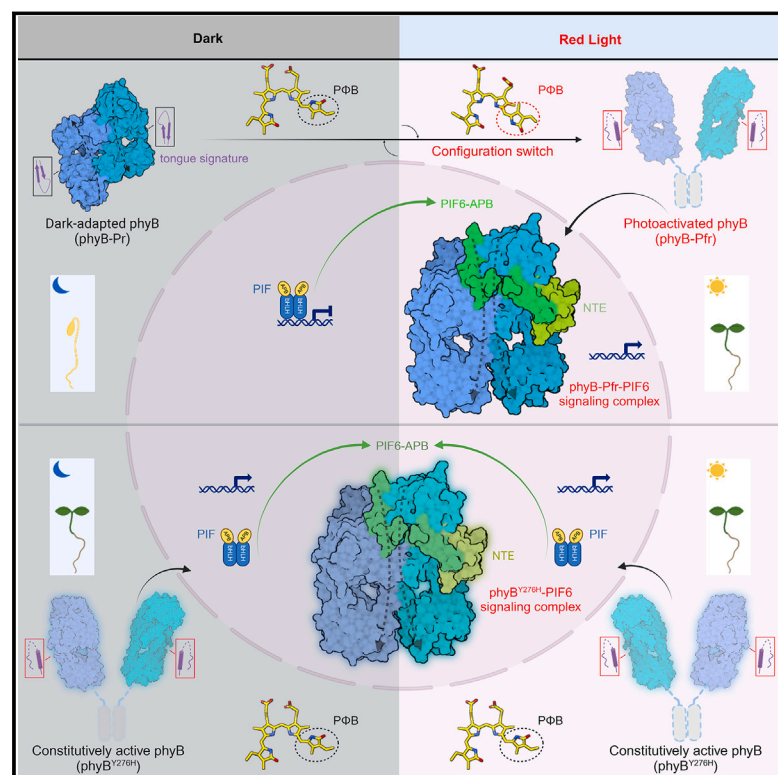# Light-induced remodeling of phytochrome B enables signal transduction by phytochrome-interacting factor

Graphical abstract

Highlights

- Red light activates phyB by remodeling the head-to-tail dimer in the dark-adapted state

- PIF6-APB binding stabilizes the NTE domain and a head-to-head dimer of activated phyB

- The asymmetric phyB dimer can accommodate only one PIF6-APB molecule

- The constitutively active phyB^{Y276H} assembles a similar trimeric complex with PIF6-APB

Authors

Zhengdong Wang, Wenfeng Wang, Didi Zhao, ..., Jun Zhao, Xing Wang Deng, Jizong Wang

Correspondence

deng@pku.edu.cn (X.W.D.), wangjizong@pku.edu.cn (J.W.)

In brief

Cryo-EM structures of *Arabidopsis* photoactivated phyB and its constitutively active phyB^{Y276H} mutant in complex with the N terminus of PIF6 provide insights into light-induced photoreceptor remodeling and signal transduction.

CellPress

Article

Light-induced remodeling of phytochrome B enables signal transduction by phytochrome-interacting factor

Zhengdong Wang,[1,2,3,5] Wenfeng Wang,[1,5] Didi Zhao,[1,5] Yanping Song,[1,2,3,5] Xiaoli Lin,[1,5] Meng Shen,[4] Cheng Chi,[1] Bin Xu,[1] Jun Zhao,[1] Xing Wang Deng,[1,2,3,*] and Jizong Wang[1,2,6,*]

[1]National Key Laboratory of Wheat Improvement, Peking University Institute of Advanced Agricultural Sciences, Shandong Laboratory of Advanced Agriculture Sciences at Weifang, Weifang, Shandong, China
[2]State Key Laboratory of Protein and Plant Gene Research, School of Advanced Agricultural Sciences, Peking University, Beijing, China
[3]Peking-Tsinghua Joint Center for Life Sciences, Peking University, Beijing, China
[4]State Key Laboratory of Plant Genomics, Institute of Genetics and Developmental Biology, Chinese Academy of Sciences, Beijing, China
[5]These authors contributed equally
[6]Lead contact
*Correspondence: deng@pku.edu.cn (X.W.D.), wangjizong@pku.edu.cn (J.W.)
https://doi.org/10.1016/j.cell.2024.09.005

SUMMARY

Phytochrome B (phyB) and phytochrome-interacting factors (PIFs) constitute a well-established signaling module critical for plants adapting to ambient light. However, mechanisms underlying phyB photoactivation and PIF binding for signal transduction remain elusive. Here, we report the cryo-electron microscopy (cryo-EM) structures of the photoactivated phyB or the constitutively active phyB^{Y276H} mutant in complex with PIF6, revealing a similar trimer. The light-induced configuration switch of the chromophore drives a conformational transition of the nearby tongue signature within the phytochrome-specific (PHY) domain of phyB. The resulting α-helical PHY tongue further disrupts the head-to-tail dimer of phyB in the dark-adapted state. These structural remodelings of phyB facilitate the induced-fit recognition of PIF6, consequently stabilizing the N-terminal extension domain and a head-to-head dimer of activated phyB. Interestingly, the phyB dimer exhibits slight asymmetry, resulting in the binding of only one PIF6 molecule. Overall, our findings solve a key question with respect to how light-induced remodeling of phyB enables PIF signaling in phytochrome research.

INTRODUCTION

Plants have evolved several families of photoreceptors to perceive distinct spectra of light signal.[1] Phytochromes (phys) are red and far-red light photoreceptors that widely exist in plants, bacteria, and fungi.[2,3] Plant phys incorporate a bilin molecule called phytochromobilin (PΦB) as a chromophore, which covalently links to a conserved cysteine residue.[4,5] Upon light irradiation, the $C_{15}=C_{16}$ double bond in PΦB undergoes isomerization, leading to the reversible conversion of phy proteins between the red-light-absorbing (Pr) and far-red-light-absorbing (Pfr) conformers, a process known as photoconversion. In the absence of light, Pfr automatically reverts back to Pr through a process called dark or thermal reversion.[6,7] In plants, Pr is localized in the cytoplasm, whereas the photoconverted Pfr translocates into the nucleus to regulate the activities of downstream partners, such as phy-interacting factors (PIFs),[8,9] or induce genome-wide changes in alternative promoter selection,[10] thereby controlling the entire life cycle of plants.

In *Arabidopsis thaliana* (*Arabidopsis*), phys are encoded by a small gene family, including *PHYA-E*.[11] Among these phys, phyB plays a dominant role in the light-grown plants.[12–14] Plant phys typically comprise an N-terminal photosensory module (PSM), a hinge region containing two tandem period/ARNT/singleminded (PAS) domains, and a histidine-kinase-related domain (HKRD).[15] The PSM is further divided into four sequential domains: N-terminal extension (NTE), N-terminal PAS (nPAS), cGMP phosphodiesterase/adenylate cyclase/FhlA (GAF), and phy-specific (PHY). Notably, the NTE and nPAS are structurally linked to the PΦB-binding GAF domain by a conspicuous knot lasso (KL) structure.[16] A helical spine links GAF to PHY, while a tongue structure from PHY extends back to GAF, abutting the PΦB-binding pocket and participating in photoconversion.[15] The PSM of phys is primarily responsible for light perception.[4,5] For phyB, both the hinge region and HKRD mediate dimerization and subcellular localization.[17,18] Furthermore, both the N and C termini of phyB are involved in signaling.[18–20] Interestingly, a mutation in the GAF domain that replaces a conserved tyrosine, which contacts PΦB, with histidine (Y276H), constitutively
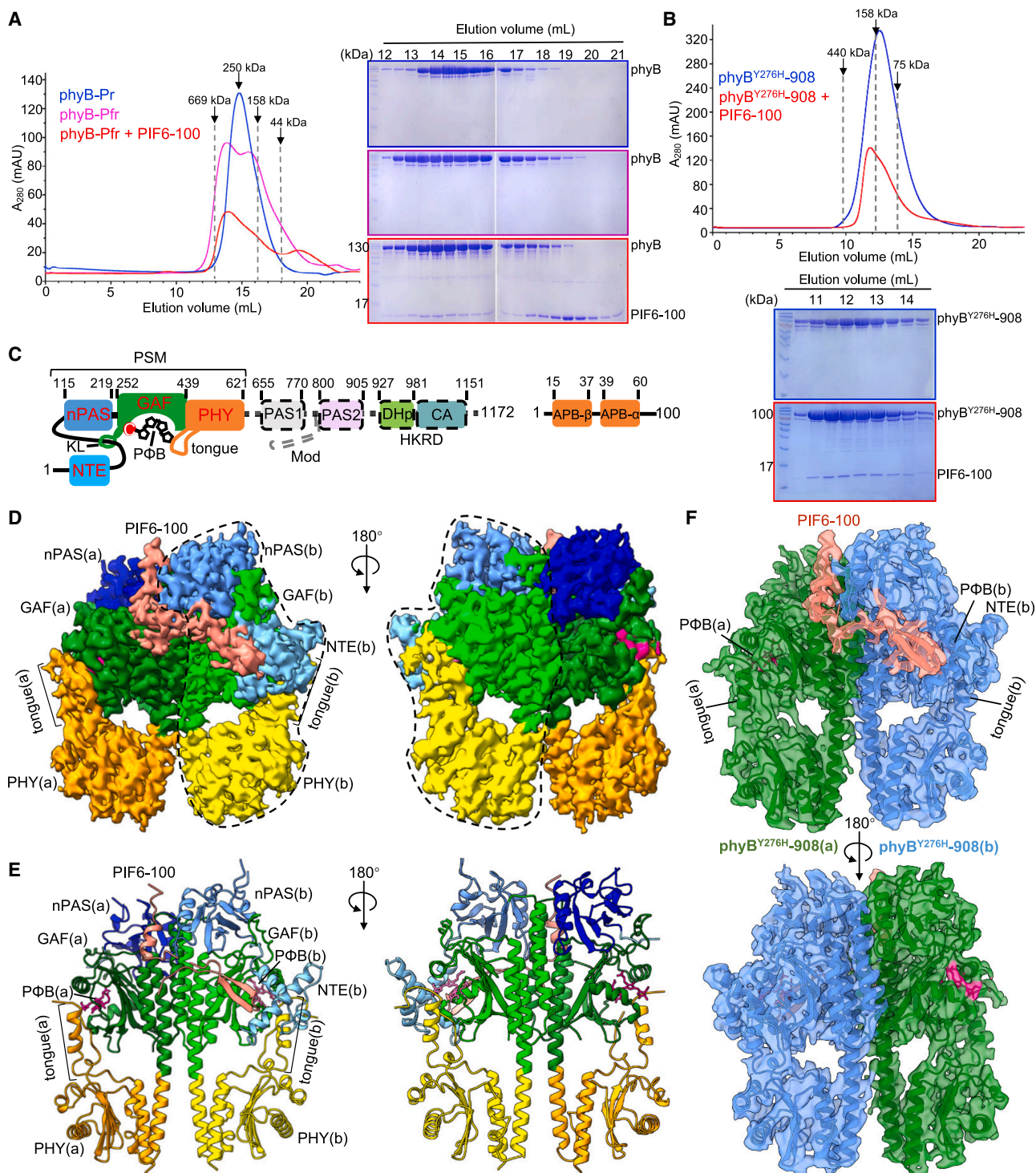
Figure 1. Overall structures of the phyB-Pfr-PIF6 and phyB^{Y276H}-908-PIF6 complexes

(A) PIF6-100 binds to phyB-Pfr. Left: gel filtration profiles of phyB-Pr (blue), phyB-Pfr (pink), and phyB-Pfr-PIF6 (red) proteins. Positions of standard molecular weights, indicated by dashed lines. Right: peak fractions in the left were visualized by SDS-PAGE followed by Coomassie brilliant blue staining.

(B) PIF6-100 binds to phyB^{Y276H}-908. Gel filtration assays of phyB^{Y276H}-908 (blue) and phyB^{Y276H}-908-PIF6 (red) proteins as described for (A).

(C) Color-coded domain architecture of full-length *Arabidopsis* phyB (left) and PIF6-100 (right). Domain boundaries are indicated by numbers.

(D) Final three-dimensional (3D) reconstruction of phyB-Pfr-PIF6 shown in two orientations. The dashed line delineates protomer-b.

(legend continued on next page)

activates phyB independent of light.[21] However, the exact mechanism by which light-induced phyB activation initiates the signaling process remains largely unknown.

The *Arabidopsis* PIF family consists of eight members, namely PIF1-8, which are classified as basic/helix-loop-helix (bHLH) transcription factors.[22–24] Dimerization and DNA binding are facilitated by the conserved bHLH domain located at the C terminus of PIFs.[8,9,25] The N termini of all PIFs contain an active-PHYB-binding (APB) motif, which primarily interacts with phyB-Pfr.[8,26] Under subterranean darkness conditions, PIFs, particularly PIF1/3/4/5, promote skotomorphogenesis, the developmental program in dark-grown seedlings that facilitates hypocotyl elongation but suppresses leaf development.[27–29] Once seedlings perceive light, activated phyB negatively regulates the aforementioned PIFs. This ultimately promotes photomorphogenesis, including the inhibition of hypocotyl elongation and cotyledon unfolding.[27–29] Upon association, phyB triggers rapid phosphorylation, ubiquitylation, and subsequent degradation of PIFs,[9,30–32] thus effectively controlling their abundance. Additionally, phyB directly interferes with the transcriptional activity of PIFs.[33,34] However, the mechanisms by which illuminated phyB recognizes PIFs and exerts specific regulatory modes remain poorly understood.

Studies of bacterial phys reveal that a light-driven configuration switch of the bilin chromophore induces a transition of PHY tongue from a β-sheet to an α-helix.[35–39] This transition results in a conformational change in the PHY domain, consequently affecting the downstream histidine kinase (HK) domain and its activity.[15,40] Although plant phys share a similar N-terminal nPAS-GAF-PHY module with their bacterial counterparts, they substantially differ in their C-terminal domains. Plant phys have additional PAS1-PAS2 hinge regions and a kinase-deficient HKRD.[15,41] As a result, plant phys recruit PIFs for signaling, whereas bacterial phys directly phosphorylate downstream substrates.[4] Recent structures of full-length phyB-Pr and phyA-Pr have revealed head-to-tail dimers mediated by PAS2 and HKRD.[42–45] However, the structures of the active Pfr form of plant phys and their signaling complexes with PIFs remain unknown. In this study, we present the structures of full-length *Arabidopsis* phyB-Pfr or the constitutively active phyB^Y276H mutant in complex with an N-terminal segment (residues 1–100) of PIF6 (PIF6-100), providing valuable insights into how a light-induced cascade of phyB remodeling enables PIF binding and signaling.

RESULTS

Reconstitution and cryo-EM reconstruction of the phyB-Pfr-PIF6 and phyB^Y276H-908-PIF6 complexes

Using a protocol for the purification of phyA protein,[45] we successfully obtained the *Arabidopsis* PΦB-bound full-length phyB and HKRD-deleted phyB^Y276H (phyB^Y276H-908) proteins. Supporting normal photoconversion, the absorption peak was observed at 662 nm in phyB-Pr and shifted to 725 nm in phyB-Pfr (Figure S1A). Additionally, phyB-Pr appeared cyan while

phyB-Pfr appeared light green. As previously reported,[46] phyB^Y276H-908 exhibited similar spectral characteristics, with a maximum absorbance at ∼662 nm, both in darkness and under red light irradiation (Figure S1B), confirming the impaired photoconversion of phyB^Y276H. Previous studies have shown that the N-terminal segment (residues 1–100) containing the conserved APB motif of PIF (PIF-100) is necessary and sufficient for binding to phyB-Pfr.[26] Indeed, all tested PIF-100 proteins, including PIF1/3/4/6, bound to full-length phyB-Pfr, albeit with varying affinities (Figure S1C). Among these PIFs, PIF6-100 showed the most robust and Pfr-specific interaction with phyB, consistent with previous findings.[26,47,48] After saturating irradiation with red light, phyB formed a stable complex with PIF6-100, as indicated by their co-migration in gel filtration (Figures 1A and S1D). Interestingly, part of the red-light-irradiated phyB eluted at positions earlier than phyB in darkness. Strikingly, phyB^Y276H-908 mainly eluted at a position of ∼100 kDa, while PIF6-100 co-migrated with phyB^Y276H-908 to a position of ∼200 kDa in gel filtration (Figures 1B and S1D).

Next, we determined the cryoelectron microscopy (cryo-EM) structures of the phyB-Pfr-PIF6 and phyB^Y276H-908-PIF6 complexes at resolutions of 3.1 and 3.2 Å, respectively (Figures 1C–1F and S1E; Data S1; Tables S1 and S2). Both structures reveal a similar trimer, consisting of a phyB dimer and a PIF6-100 monomer. Unexpectedly, only the N-terminal PSM is well defined in the cryo-EM structures, whereas the C-terminal PAS2 and HKRD domains, which mediate a tightly packed head-to-tail PSM dimer in the phyB-Pr structure, are completely flexible.[42] Furthermore, the PIF6-bound phyB-Pfr or phyB^Y276H-908 forms a head-to-head PSM dimer (Figures 1C–1F). PIF6-100 binds to both PSM modules of phyB-Pfr or phyB^Y276H-908. The N-terminal portion of PIF6-100 folds into a β-hairpin structure and binds to one phyB protomer. This part of APB was therefore designated APB-β, and its recognizing phyB protomer is called phyB(b), with the other being referred to as phyB(a). By comparison, the C-terminal part of PIF6-100, designated APB-α, forms an α-helix and is sandwiched between two phyB protomers (Figures 1C–1F). Interestingly, PIF6-100 only binds to one side of the phyB dimer (Figures 1D–1F), resulting in a 2:1 stoichiometry of phyB-Pfr or phyB^Y276H-908 and PIF6-100.

Light-triggered configuration switch of PΦB results in an α-helical PHY tongue

To probe the light-induced remodeling of the N-terminal PSM of phyB, we compared the structures of the PSM of phyB-Pr and phyB-Pfr. The alignment revealed a slight shift in the nPAS domain and its interacting portion of KL in the GAF domain, while the majority of GAF remains unchanged (Figure 2A; Data S1). Similar to phyB-Pr,[42] the 150s loop (residues 145–155) in nPAS and the 380s loop (residues 381–391) in GAF of phyB-Pfr remain flexible. Notably, there is a distinct rotation of the PHY domain along the helical spine in phyB-Pfr (Figure 2A; Data S1). As observed in bacterial phys,[35–39,49,50] the PHY tongue undergoes a noticeable transition from a β-sheet in phyB-Pr to an α-helix in

---

(E) Model of phyB-Pfr-PIF6 shown in two orientations.

(F) Cryo-EM map of phyB^Y276H-908-PIF6 superposed with an atomic model in cartoon, shown in two orientations.
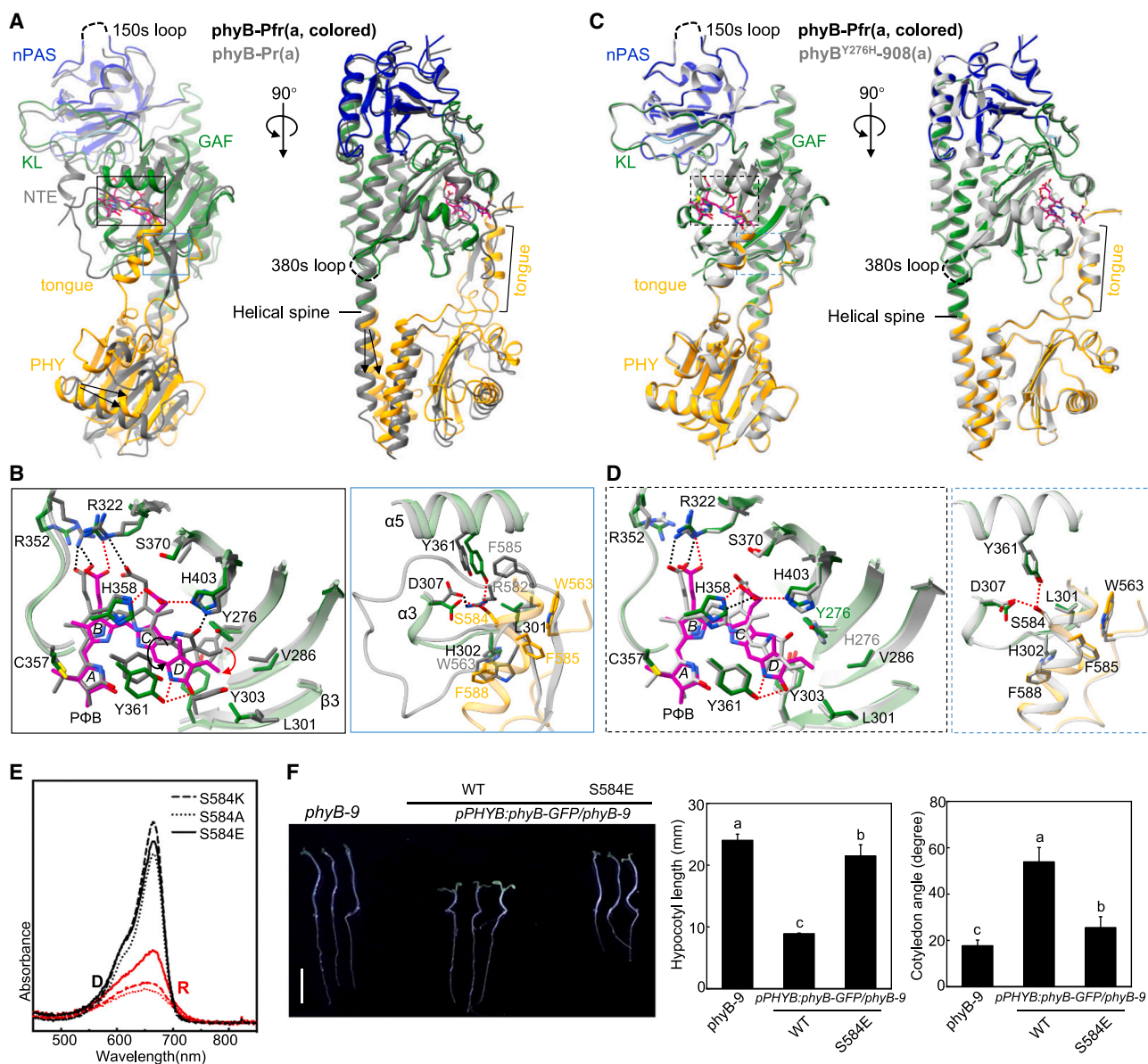
See also Figure S1, Data S1, and Tables S1 and S2.

Figure 2. Light-induced transition of the PHY tongue

(A) Structural comparison of the PSM of phyB-Pfr (color-coded) and phyB-Pr (dark gray, PDB: 7RZW), shown in two orientations. Arrows indicate the rotation of helical spine or PHY domain.

(B) Left: details of the PΦB-binding pocket in GAF of phyB-Pfr (green) and phyB-Pr (dark gray), indicated by black box in (A). PΦB of Pfr shown in magenta. Hydrogen bonds indicated by red (Pfr) or black (Pr) dashed lines. Black arrow indicates the flipping of D-ring; red arrow indicates the sliding of PΦB. Right: details of interactions between the PHY tongue (yellow) and PΦB-binding pocket in GAF (green) of phyB-Pfr and phyB-Pr (dark gray), indicated by blue box in (A).

(C) Structural comparison of the PSM of phyB-Pfr (color-coded) and phyB[Y276H] (light gray), shown in two orientations.

(D) Close-up views of interactions highlighted in (C) as described for (B).

(E) UV-vis absorbance spectra of phyB[S584E], phyB[S584A], and phyB[S584K] proteins in the dark (D), and after saturating irradiation with red light (R).

(F) *PHYB[S584E]* failed to recover *PHYB* functions in *phyB-9* seedlings. Left: representative seedlings grown for 5 days under continuous red light (Rc). Statistics on hypocotyl length (middle) and cotyledon angle (right). Scale bar, 1 cm. Mean ± SD, n ≥ 20.

See also Figure S2 and Data S1 and S2.

phyB-Pfr (Figure 2A; Data S1), while the rest of PHY remains almost identical (Figure S2A).

In comparison with PΦB in phyB-Pr, which adopts a 5(*Z*)*syn*-10(*Z*)*syn*-15(*Z*)*anti* configuration,[42,46,51] both PΦB molecules in

phyB-Pfr assume a 5(*Z*)*syn*-10(*Z*)*syn*-15(*E*)*anti* configuration, with the D pyrrole ring flipped 180° (Figures 2B and S2B; Data S1). Simultaneously, PΦB slides to a different position within the GAF pocket and establishes new contacts with phyB-Pfr

(Figure 2B; Data S1). Notably, dramatic changes occur in the rotamers of Y276, L301, Y303, and Y361 to accommodate the new conformation of PΦB, which potentially drives the transition of the PHY tongue. Specifically, in Pr, the PHY tongue contacts the PΦB-binding pocket in the GAF domain via interactions with L301, Y303 in strand-β3, D307 in helix-α3, and Y361 in helix-α5 (Figure 2B). These interactions are disrupted by the conformational changes in these residues in Pfr, and the new conformation of Y361 is predicted to cause steric clash with F585 in Pr, further facilitating the transition of the PHY tongue. Additionally, the formation of a bifurcated hydrogen bond of S584 with D307 and Y361 helps stabilize the conformation of the α-helical PHY tongue in Pfr (Figure 2B). Structural comparison also reveals substantial similarity between the PSM of phyB-Pfr and that of the bacteriophytochrome from *Deinococcus radiodurans* (DrBphP) (Figures S2C–S2G).[39] These structural observations collectively support a conserved mechanism of the light-driven transition of the PHY tongue from a β-sheet to an α-helix in different phy species.

Further supporting the light-induced α-helical PHY tongue in phyB-Pfr, structural comparison reveals that the structure of the constitutively active phyB^{Y276H} is almost identical to that of phyB-Pfr (Figures 2C and S2H). Consistent with the spectral data, the PΦB in phyB^{Y276H} adopts a 5(Z)syn-10(Z)syn-15(Z) anti configuration similar to phyB-Pr (Figures 2D and S1B; Data S1). However, the position of PΦB, located within the binding pocket of phyB^{Y276H}, differs substantially from that in phyB-Pr but resembles that in phyB-Pfr (Figures 2D, S2I, and S2J). Furthermore, almost the same set of contacts are formed between PΦB and phyB^{Y276H} as those in phyB-Pfr (Figure 2D; Data S1). Notably, H276 adopts a conformation similar to Y276 in phyB-Pfr, which is predicted to clash with the PΦB in phyB-Pr (Figures 2B and 2D). This presumably triggers the sliding of PΦB as observed in phyB-Pfr, leading to the formation of a similar α-helical PHY tongue.

Supporting the critical role of S584 in stabilizing the α-helical PHY tongue of phyB-Pfr or phyB^{Y276H}, the S584E mutation eliminates the Pr-to-Pfr photoconversion of the phyB-PSM proteins.[46] We additionally introduced various mutations to this residue, including S584E, S584A, and S584K, and purified the full-length phyB mutant proteins (Data S2). Similarly, red light irradiation had no impact on the absorbance at 725 nm of these mutant proteins (Figure 2E). To assess the biological significance of this residue, we generated transgenic *phyB-9* plants expressing wild-type (WT) *PHYB* or *PHYB^{S584E}*. Expression of *PHYB^{WT}* led to shorter hypocotyl and relatively open cotyledons in the mutant plants (Figures 2F and S2K), whereas no effect was observed upon expression of *PHYB^{S584E}*. In conclusion, PΦB-induced transition of the PHY tongue is crucial for phyB signaling.

The α-helical PHY tongue promotes phyB remodeling

Because of an asymmetric dimer of phyB-Pr,[42] the structures of the two protomers of phyB-Pr and phyB-Pfr were individually aligned to examine conformational changes in phyB induced by the α-helical PHY tongue (Figures 3A and 3B). As discussed earlier, the C-terminal PAS2 and HKRD domains mediating the head-to-tail dimer of N-terminal PSM in phyB-Pr become flexible

in phyB-Pfr (Figures 1D–1F).[42] This structural observation aligns with the data indicating that alterations in a loop region known as the modulator loop (Mod), connecting the PAS2 and PHY domains, disrupt the PAS2-mediated dimerization of phyB-Pr while promoting the stability of phyB-Pfr.[42] In phyB-Pr, the Mod assumes a β-hairpin structure and packs against the PHY β-sheet. The tip of the β-hairpin projects toward the PHY tongue (Figures 3A and 3B). Structural comparison shows that the α-helical PHY tongue in phyB-Pfr clashes severely with this tip (Figures 3A–3C and S3A). This clash triggers conformational changes in the Mod during the Pr-to-Pfr conversion, which subsequently disturb the Mod-PHY interaction and cause a rotation of the PHY domain (Figures 3A and S3B). Consequently, the intramolecular contacts between the C-terminal PAS2 and N-terminal PHY are impaired. Overall, these structural observations demonstrate that PΦB-induced transition of the PHY tongue results in the disruption of the PAS2-mediated dimerization of phyB-Pr and promotes phyB remodeling.

As discussed above, the PHY domain clearly rotates during the Pr-to-Pfr conversion (Figures 2A and 3A). This striking conformational change causes clashes between a loop region in the PHY domain and a loop region N-terminal to strand-β1 of the HKRD domain in phyB(a) (Figures 3A, 3C, and S3C), cancelling the intramolecular interaction between HKRD and PHY in this protomer. Additionally, a noticeable conformational change occurs in the N-terminal side of GAF-α1 of phyB(b) upon photoactivation. Compared with the curved GAF-α1 in phyB-Pr, this α-helix becomes straight in phyB-Pfr (Figure 3B). The straightened GAF-α1 collides with the helix-α3 and its C-terminal loop of HKRD (Figures 3D and S3C), eliminating the intramolecular HKRD-GAF interaction in phyB(b). Altogether, the contacts between the distal C-terminal HKRD and the N-terminal PSM in phyB-Pr are disrupted in phyB-Pfr.

Previous biochemical data indicated that a HKRD-deleted version of phyB (phyB-908) mainly exists as a PAS2-mediated dimer in the dark.[42] Our biochemical data showed that the phyB-908 protein largely eluted at approximately 100 kDa after red light irradiation in gel filtration (Figures 3E, S3D, and S3E), indicating a monomeric size similar to the activated phyB^{Y276H}-908 (Figure 1B). Moreover, the PAS2 domain exhibits flexibility in phyB^{Y276H}-908, resembling phyB-Pfr (Figures 2C and S2H). Overall, our data indicate that the α-helical PHY tongue promotes the further remodeling of phyB, disrupting the interactions between the N and C termini.

Molecular mechanism of PIF6-100 recognition by phyB

Previous studies have indicated that the PSM of phyB-Pfr is both necessary and sufficient for binding full-length PIF or PIF-100.[26,48,52,53] Furthermore, forced nuclear localization of phyB-PSM results in the activation of phyB responses.[19] Consistent with these data, PSM is involved in both PIF-100 recognition and phyB-Pfr or phyB^{Y276H}-908 dimerization (Figure 4A). Because the structures of phyB-Pfr-PIF6 and phyB^{Y276H}-908-PIF6 are almost congruent (Figures S2H and S4A), we used the former for analysis in the following sections. In the cryo-EM structure, the N-terminal APB-β (residues 15–37) of PIF6-100 binds to the NTE-nPAS-GAF module of phyB(b), while the C-terminal APB-α (residues 39–60) is sandwiched between the GAF
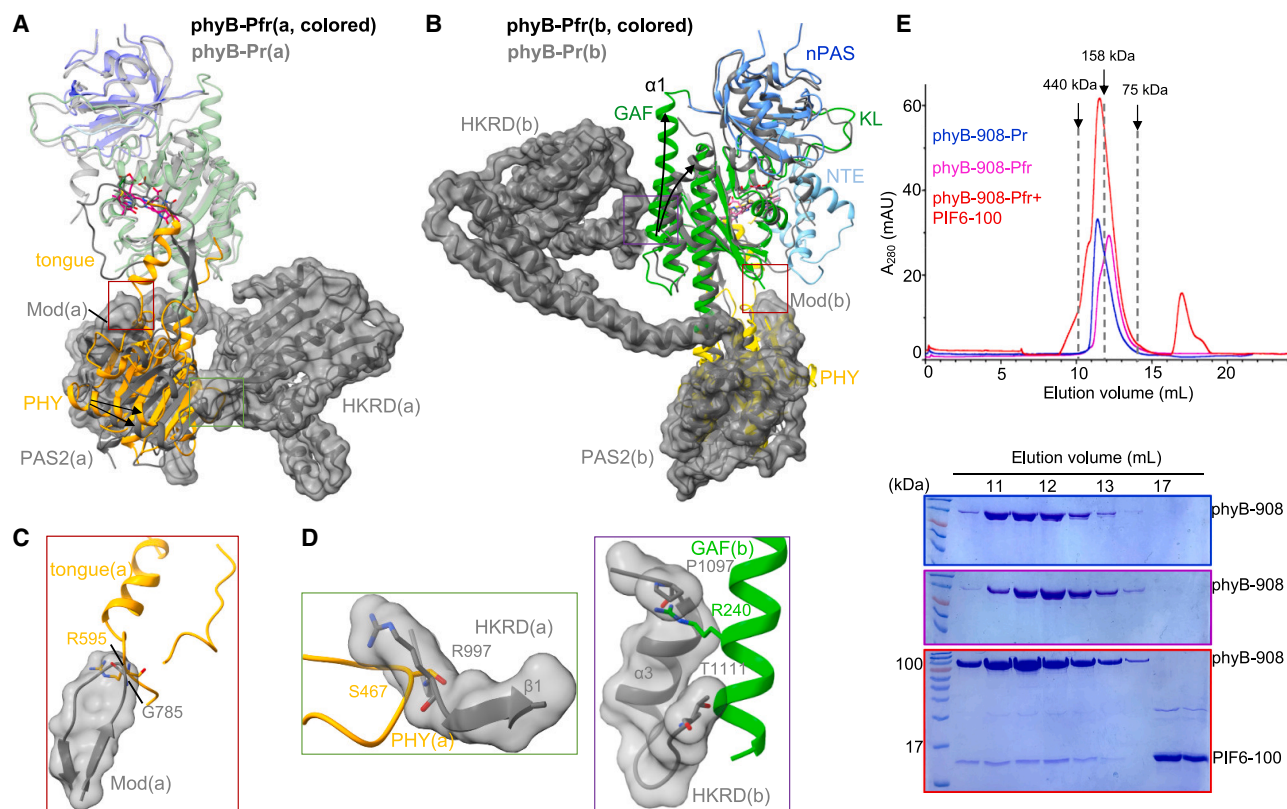
Figure 3. The α-helical PHY tongue promotes phyB remodeling for activation

(A) Structural comparison of protomer-a of phyB-Pfr (color-coded) and phyB-Pr (gray, PDB: 7RZW). The PAS2-HKRD module in phyB-Pr, shown in surface. Arrows indicate the rotation of PHY domain.

(B) Structural comparison of protomer-b of phyB-Pfr (color-coded) and phyB-Pr (gray, PDB: 7RZW). Arrows indicate the orientation of GAF-α1.

(C) Details of clashes between α-helical PHY tongue (yellow) and Mod of PAS2 (gray), indicated by red box in (A) and (B).

(D) Left: details of clashes between PHY (yellow) and HKRD (gray), indicated by green box in (A). Right: details of clashes between GAF (green) and HKRD (gray), indicated by purple box in (B).

(E) Red light irradiation disrupts phyB-908 dimerization, which is recovered by PIF6-100. The assays were performed as described for Figure 1A.

See also Figure S3.

domain of phyB(a) and the nPAS domain of phyB(b) (Figure 4A; Data S1). Specifically, E19, L20, and Q32 of PIF6-APB-β form an extensive hydrogen bond network with NTE-Q109, NTE-R110, KL-C345, and nPAS-D209 (Figure 4B; Data S1). Notably, L20, F22, and I27 at the tip of PIF6-APB-β tightly pack against GAF-F314, NTE-L105, NTE-I101, and NTE-Y61 through hydrophobic interactions. G25 is located within the β-turn and serves as a common marker for stabilizing the overall structure of the APB-β-hairpin (Figure 4B). The PIF6-APB-α establishes extensive contacts with the α1, α2, and α6 helices of the GAF domain in phyB(a), as well as the helix-α3 and its following loop of the nPAS domain in phyB(b) through hydrogen bonds and electrostatic and hydrophobic interactions (Figure 4C; Data S1). A small fragment (residues 10–14) N-terminal to APB-β also contacts GAF-α1, GAF-α2 of phyB(a), and the nPAS loop of phyB(b) (Figure 4C).

To verify the structural mechanism mentioned above, we generated truncated versions of PIF6-100 and evaluated their interaction with phyB through pull-down assays. APB-β (residues 15–37) was able to interact with phyB-Pfr but exhibited

substantially lower affinity than PIF6-100 (Figure 4D; Data S2). PIF6 (residues 1–37) displayed a similar affinity to phyB-Pfr, suggesting that the very N-terminal 14 residues are dispensable for phyB-PIF6 interaction. Removal of the disordered C-terminal segment of PIF6-100 (residues 65–100), indicated by the cryo-EM structures, did not affect the phyB-PIF6 interaction (Figure 4D; Data S2). Consistent with previous findings,[26,47] mutations in key residues of APB-β abolished or severely compromised the PIF6- or PIF3-phyB interaction (Figures 4E, S4B, and S4C; Data S2), further supporting a critical role of this conserved region of PIF-APB in binding phyB. Sequence alignment demonstrated that the key residues in APB-α are weakly conserved among other PIFs (Figure S4D). Hence, the region containing APB-α in PIFs potentially contributes to the varying affinities of different PIFs for phyB (Figure S1C).

To assess the importance of phyB residues that contact the conserved APB-β, we generated phyB[I101E], phyB[Q109A/R110A], phyB[F314A], and phyB[Q318A] mutants and examined their interactions with PIF6-100 using pull-down assays. In full support of the cryo-EM structures, the first three mutants did not bind
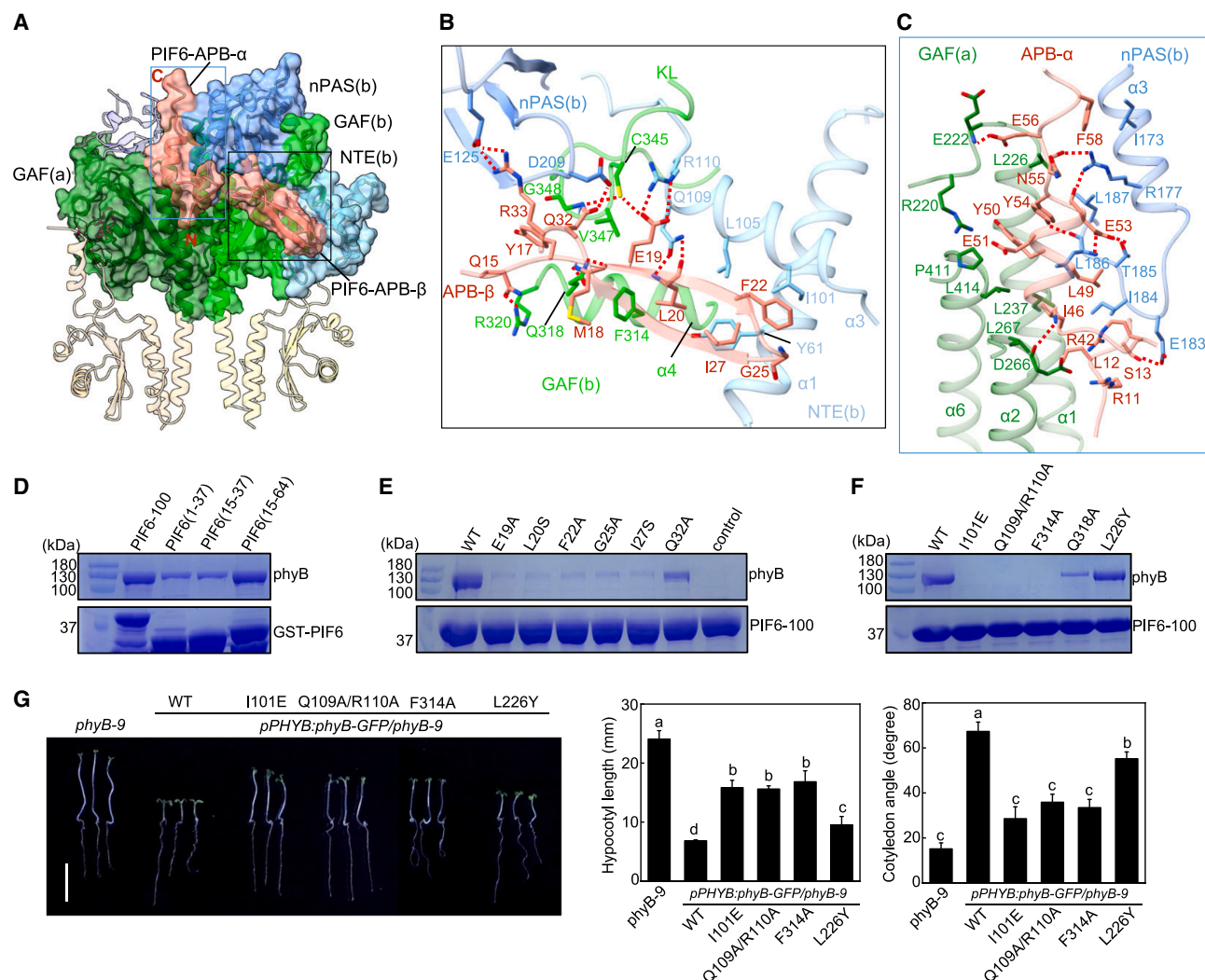
Figure 4. Recognition of PIF6-100 by phyB-Pfr

(A) Domains of phyB-Pfr recognizing PIF6-APB-β and PIF6-APB-α, shown in colored surface.

(B) Details of PIF6-APB-β recognition, indicated by black box in (A).

(C) Details of PIF6-APB-α recognition, indicated by blue box in (A).

(D) GST-tagged PIF6 bound to GS4B beads were incubated with an excess amount of full-length phyB under Rc. After extensive washing, the beads were analyzed by SDS-PAGE and Coomassie brilliant blue staining.

(E) Mutations of PIF6-APB-β around the interface shown in (B) affected the phyB-PIF6 interaction, as assayed in (D).

(F) Mutations of phyB around the interface shown in (B) and (C) affected the phyB-PIF6 interaction, as assayed in (D).

(G) *PHYB* mutations that reduce the PIF6-binding activity impaired phyB signaling, as assayed in Figure 2F.

See also Figure S4 and Data S1 and S2.

PIF6-100, whereas phyB^{Q318A} was strongly impaired in PIF6 interaction (Figure 4F; Data S2). Conversely, the L226Y mutation in phyB, predicted to compromise contact with APB-α, marginally reduced the phyB-PIF6 interaction. Consistent with these biochemical data, expression of *PHYB^{I101E}*, *PHYB$^{Q109A/R110A}$*, or *PHYB^{F314A}* failed to fully rescue phyB functions in transgenic *phyB-9* plants (Figure 4G). These mutations had no impact on the level or nuclear localization of the mutant proteins but attenuated the stability of photobodies in seedlings (Figures S4E and S4F). In comparison, *phyB-9* seedlings expressing *PHYB^{L226Y}* exhibited shorter hypocotyls and relatively

open cotyledons, indicating a moderate effect of this mutation on phyB function.

NTE has a dual role in recognizing PIF6-APB-β and stabilizing phyB-Pfr

As discussed above, NTE directly recognizes PIF6-APB-β (Figure 4B). Structural comparison between phyB-Pfr and phyB-Pr reveals a striking remodeling of the NTE upon PIF6-APB-β binding. NTE assumes a short α-helix in phyB-Pr, folding into three α-helices (α1–α3) in phyB-Pfr when binding PIF6-APB-β (Figure 5A; Data S1). Furthermore, the NTE-α3 in phyB(b) becomes
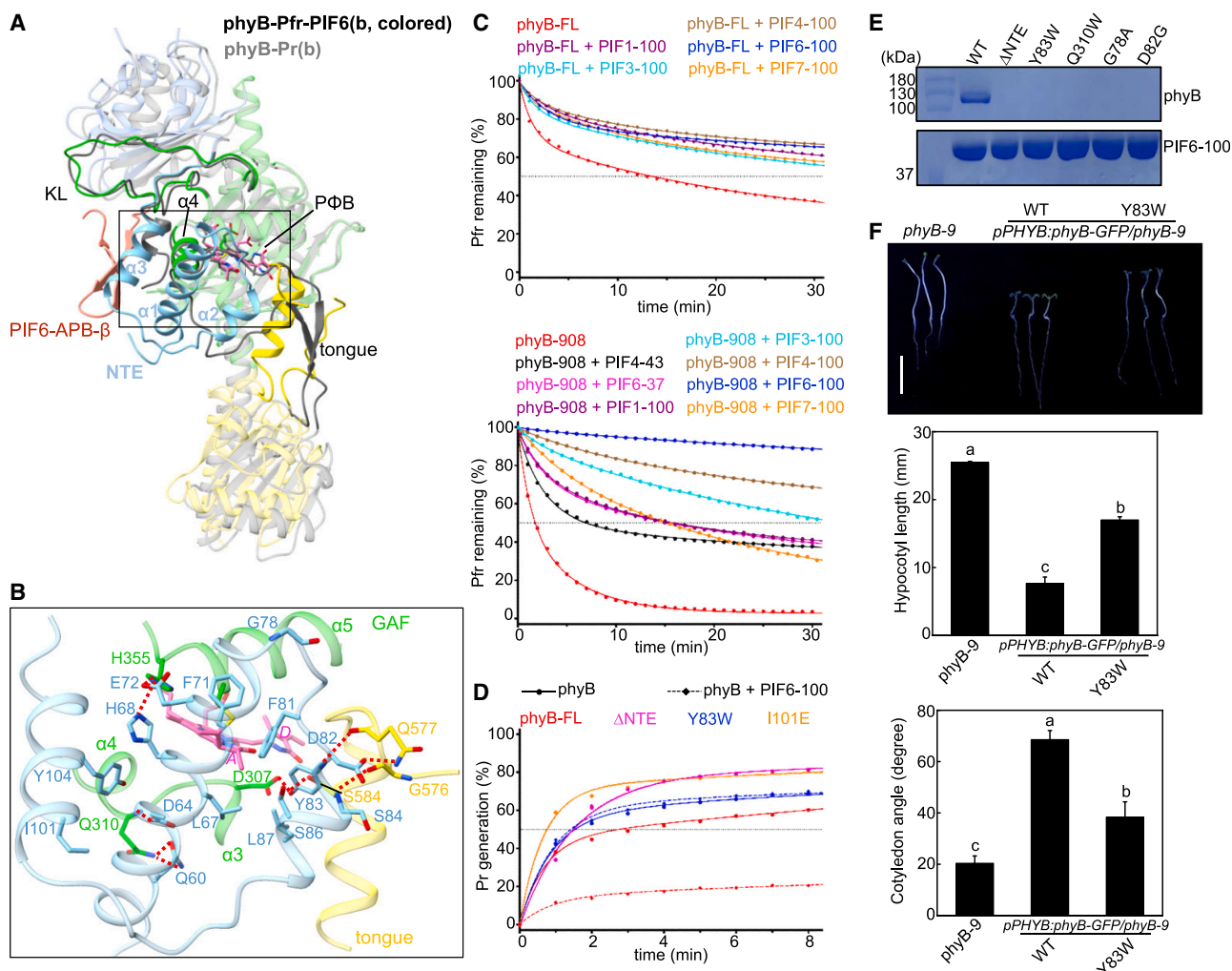
Figure 5. NTE is involved in specific recognition of PIF6-APB-β and stabilization of phyB-Pfr

(A) Structural comparison of PIF6-APB-β-bound phyB-Pfr (color-coded) and phyB-Pr (gray, PDB: 7RZW).

(B) Details of NTE-mediated intramolecular interactions, indicated by black box in (A).

(C) PIF1/3/4/6/7-APB effectively inhibit the dark reversion of full-length phyB (top) and phyB-908 (bottom). The phyB samples, with or without PIF, were photoconverted to Pfr and allowed to revert back to Pr at 22°C in the dark. Normalized data points indicate reversion measurements at 725 nm and representative of three technical replicates.

(D) Mutations that disrupt NTE-mediated intramolecular interactions accelerate phyB dark reversion and eliminate the PIF6-mediated inhibition of phyB dark reversion. The assays were performed as described for (C). Pr generation was utilized to assess phyB dark reversion due to the compromised photoconversion of these phyB mutants, as illustrated in Figure S5A. Normalized data points indicate reversion measurements at 660 nm.

(E) Mutations that disrupt NTE-mediated intramolecular interactions eliminated the phyB-PIF6 interaction, as assayed in Figure 4D.

(F) PHYB^Y83W failed to fully rescue phyB responses, as assayed in Figure 2F.

See also Figure S5 and Data S1 and S2.

extended and bends outward compared with that in phyB-Pr. Considering that GAF-α4 and GAF-KL undergo no striking conformational changes following PIF6-APB-β binding (Figure 5A), NTE-α1 and NTE-α3 form the exclusive binding site for phyB-Pfr to recognize PIF6-APB-β. These structural observations indicate that NTE enables specific recognition of PIF6 by phyB-Pfr.

In addition to binding PIF6-APB-β, NTE also forms extensive intramolecular interactions by contacting PΦB and its binding pocket, as well as the PHY tongue in phyB(b) (Figure 5B), indi-

cating that the newly formed NTE has a role in stabilizing the Pfr state of this phyB protomer. Specifically, several hydrophobic residues, including L67, F71, F81, and L87 from NTE-α1, NTE-α2, and their connecting loop, directly contact the hydrophobic side of the A-ring of PΦB (Figure 5B; Data S1). NTE-α1 is anchored to GAF-α4 and GAF-α5 through hydrogen bonding with Q310 and H355, respectively, while NTE-α2 establishes hydrogen bonds mainly with the PHY tongue via D82, Y83, and S84. Notably, Y83 forms a bifurcated hydrogen bond with D307 in GAF-α3 and S584 in the PHY tongue (Figure 5B).
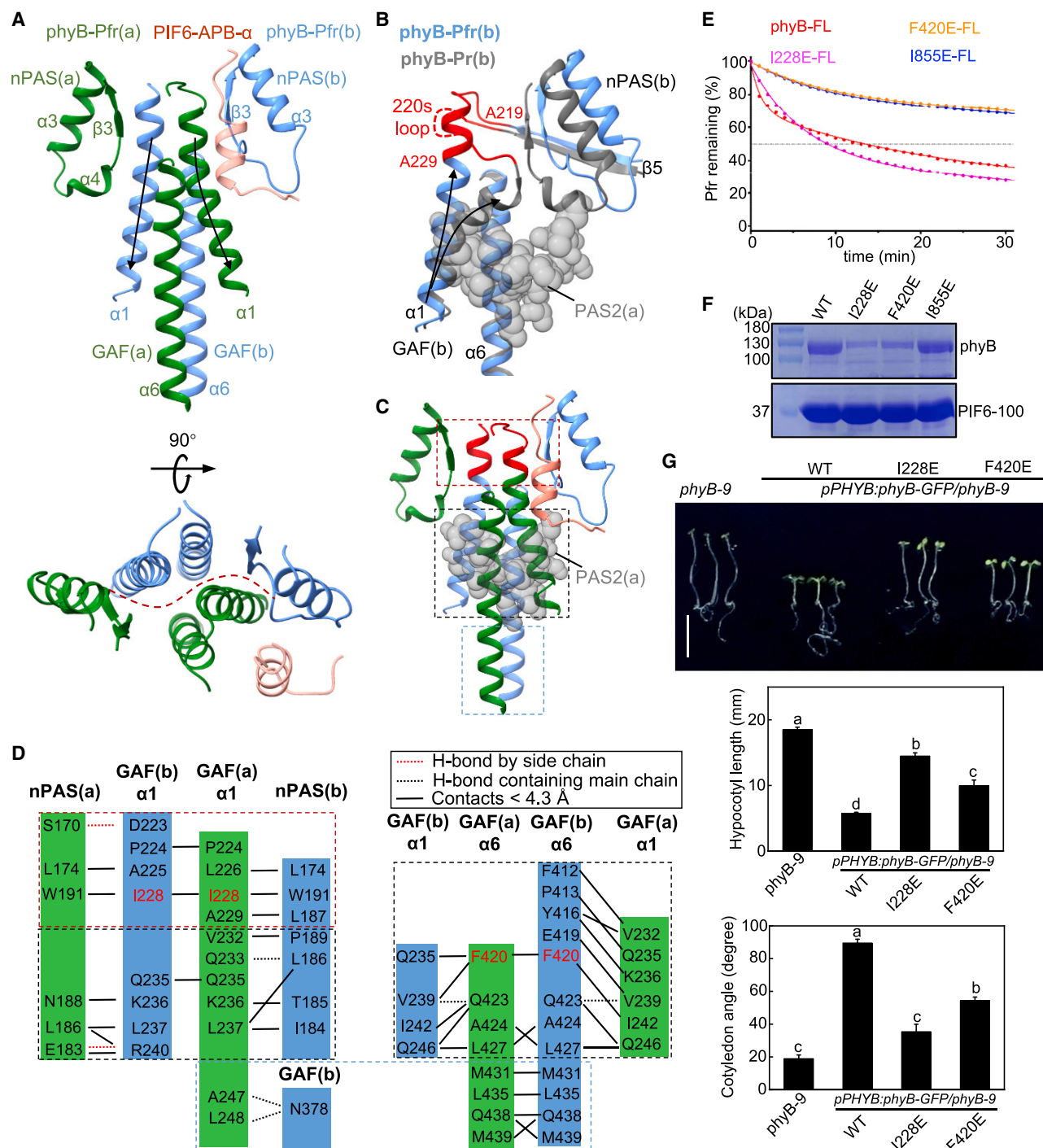
Figure 6. A head-to-head dimer of phyB-Pfr stabilized by PIF6-APB-α for signaling

(A) The nPAS-GAF module in phyB-Pfr that mediates the head-to-head dimerization of PSM, shown in side and top views. PIF6-APB-α binds to one side of the dimerization interface. Arrows indicate the orientation of GAF-α1.

(B) Structural comparison of the nPAS-GAF module of phyB-Pfr (blue) and phyB-Pr (gray, PDB: 7RZW). The PAS2 domain from the other phyB-Pr protomer, shown in sphere. The 220s loop colored in red. Arrows indicate the orientation of GAF-α1.

(C) Disruption of PAS2-mediated interactions in phyB-Pr enables the head-to-head dimerization by the nPAS-GAF module in phyB-Pfr. The newly formed N-terminal portion of GAF-α1 colored in red.

(D) Details of interactions within dimerization interface, indicated by dashed line boxes in (C).

(E) Mutations on the dimerization interface of phyB-Pfr or phyB-Pr differently affected phyB dark reversion, as assayed in Figure 5C.

(legend continued on next page)

Despite these intramolecular interactions, the NTE in phyB(a) with no PIF6-APB-β binding is flexible (Figures 1D–1F and 2A; Data S1), suggesting that the NTE remodeling is induced by PIF6-APB-β binding. This raises the question of why the PIF6-APB-β-induced remodeling of NTE only occurs in phyB-Pfr. Structural comparison shows that the PHY tongue of phyB-Pr is positioned to overlap with NTE-α1 and NTE-α2 in phyB-Pfr (Figure 5A), thus preventing the NTE remodeling. Together, these structural observations suggest that the light-induced transition of the PHY tongue acts as a prerequisite for an induced-fit recognition of PIF6-APB-β by the phyB-NTE.

To further investigate the role of PIF6-100 and other PIF-100s in stabilizing phyB-Pfr, their effects on phyB dark reversion were examined. As expected, PIF6-100 greatly hindered the Pfr-to-Pr dark reversion of full-length phyB or phyB-908 (Figure 5C). Similarly, PIF1/3/4/7-100, with varying phyB-binding activities, showed different degrees of inhibition on phyB dark reversion (Figures 5C and S1C). PIF6 (residues 1–37) and PIF4 (residues 1–43) also considerably retarded phyB dark reversion (Figures 5C and S4D), indicating that the APB-β motif has a conserved role in stabilizing phyB-Pfr. However, their inhibitory efficiency was lower than that of PIF6-100 or PIF4-100, supporting a role for the APB-α motif in stabilizing phyB-Pfr.

To determine whether NTE remodeling is required for APB-β binding and the consequent stabilization of phyB-Pfr, truncations or site-directed mutations were introduced into phyB to disrupt NTE-mediated intramolecular interactions. Supporting the structural observations, all these NTE mutants displayed accelerated reversion rates (Figures 5D and S5A), similar to the NTE-deleted version of phyB-PSM (Figure S5B).[46,54,55] Notably, these NTE mutants no longer responded to the PIF6-induced inhibition of phyB dark reversion (Figures 5D and S5B), indicating the importance of NTE-mediated intramolecular interactions in stabilizing phyB-Pfr. Interestingly, these NTE mutations abolished the phyB-PIF6 interaction (Figures 5E and S5C), supporting the requirement of NTE remodeling for binding PIF6. *In vivo* study showed that *phyB-9* seedlings expressing *PHYB^Y83W* containing a mutation in the NTE still exhibited long hypocotyls and closed cotyledons, indicating impaired phyB responses (Figures 5F, S5D, and S5E). Intriguingly, fewer photobodies were observed in these transgenic seedlings compared with those expressing *PHYB^WT*. In summary, the data indicate that the NTE controls the specific recognition of PIF-APB-β by phyB-Pfr for phyB signaling.

Head-to-head dimerization of the PIF6-100 bound phyB-Pfr

The PSM-mediated phyB-Pfr dimerization is necessary for triggering physiological responses.[19,56] Supporting this conclusion, the cryo-EM structure revealed a head-to-head dimer of phyB-Pfr mediated by both PSM and PIF6-100 (Figures 1D, 1E, 4A, and 4C). PSM contributes to phyB-Pfr dimerization through GAF-α1 and GAF-α6 of the two protomers, which form a four-he-

lix bundle (Figure 6A). Additionally, an nPAS segment packs between the protomers against GAF-α1, further stabilizing the four-helix bundle. Structural comparison shows that the PAS2 domain in phyB-Pr interacts with the same nPAS-GAF module, mediating a head-to-tail dimer (Figures 6B, S6A, and S6B).[42] In phyB-Pfr, PAS2 becomes flexible, allowing the nPAS-GAF module to mediate the head-to-head dimerization (Figure 6C). Compared with phyB-Pr, the nPAS-GAF module in phyB-Pfr undergoes conformational changes. The loop connecting the nPAS and GAF domains, designated 220s loop (residues 219–229), becomes well defined and partially folds into GAF-α1, resulting in an extended and straightened GAF-α1 in phyB-Pfr (Figure 6B; Data S1). The newly formed N-terminal portion of GAF-α1 participates in both phyB-PSM dimerization and PIF6-APB-α binding (Figure 6C). Hydrophobic contacts dominate the PSM dimerization in phyB-Pfr (Figure 6D). Intriguingly, residues of nPAS or GAF-α6 that interact with GAF-α1 in the other protomer vary considerably between phyB(a) and phyB(b), indicating that the phyB-PSM dimer is asymmetric.

Despite multiple inter-protomer interactions (Figure 6D), the Pfr proteins of phyB-PSM or phyB-908, as well as phyB^Y276H-908, mainly exist as monomers in solution (Figures 1B and 3E).[19,46,51] However, PIF6-100 co-migrated with photoactivated phyB-908 or phyB^Y276H-908 and eluted at a position close to a dimeric size (Figures 1B and 3E), indicating that PIF6-100 promotes dimerization of phyB-908-Pfr or phyB^Y276H-908. Structural observations also indicate that PIF6-APB-α binds to the PSM-mediated dimerization interface (Figures 4C and 6A). Taken together, these findings suggest an induced-fit recognition mechanism in which PIF6-APB-α binds to and stabilizes a head-to-head dimer of phyB-Pfr upon light-induced disruption of the PAS2-mediated head-to-tail dimer of phyB-Pr.

To verify the structural observations, I228E, F420E, and I855E mutations were generated. I228 in GAF-α1 and I855 in PAS2 are exclusively involved in phyB-Pfr and phyB-Pr dimerization, respectively (Figures 6C and 6D), whereas F420 in GAF-α6 participates in both phyB-Pr and phyB-Pfr dimerization. Consistently, I228E moderately accelerated the dark reversion of phyB, while F420E and I855E, which are predicted to destabilize phyB-Pr, strongly inhibited phyB dark reversion (Figures 6E and S6C).[42] Interestingly, I228E and F420E, which are predicted to impair the phyB-Pfr dimerization, substantially compromised the phyB-PIF6 interaction (Figures 6F and S6D). By comparison, phyB^I855E bound PIF6-100 similarly to phyB^WT. Supporting these biochemical data, expression of *PHYB^I228E* failed to fully rescue phyB responses in *phyB-9* mutant background, while *PHYB^F420E* recovered phyB functions more effectively than *PHYB^I228E*, presumably due to reduced dark reversion (Figures 6G, S6E, and S6F). Furthermore, the number of photobodies in these two types of transgenic seedlings decreased to varying extents compared with *PHYB^WT*-expressing seedlings. In conclusion, PIF6-APB-α binds to and stabilizes the head-to-head dimer of phyB-Pfr for phyB signaling.

(F) Mutations on the dimerization interface of phyB-Pfr impaired the phyB-PIF6 interaction, as assayed in Figure 4D.

(G) *PHYB* mutations that impair phyB-Pfr dimerization reduced phyB responses, as assayed in Figure 2F.
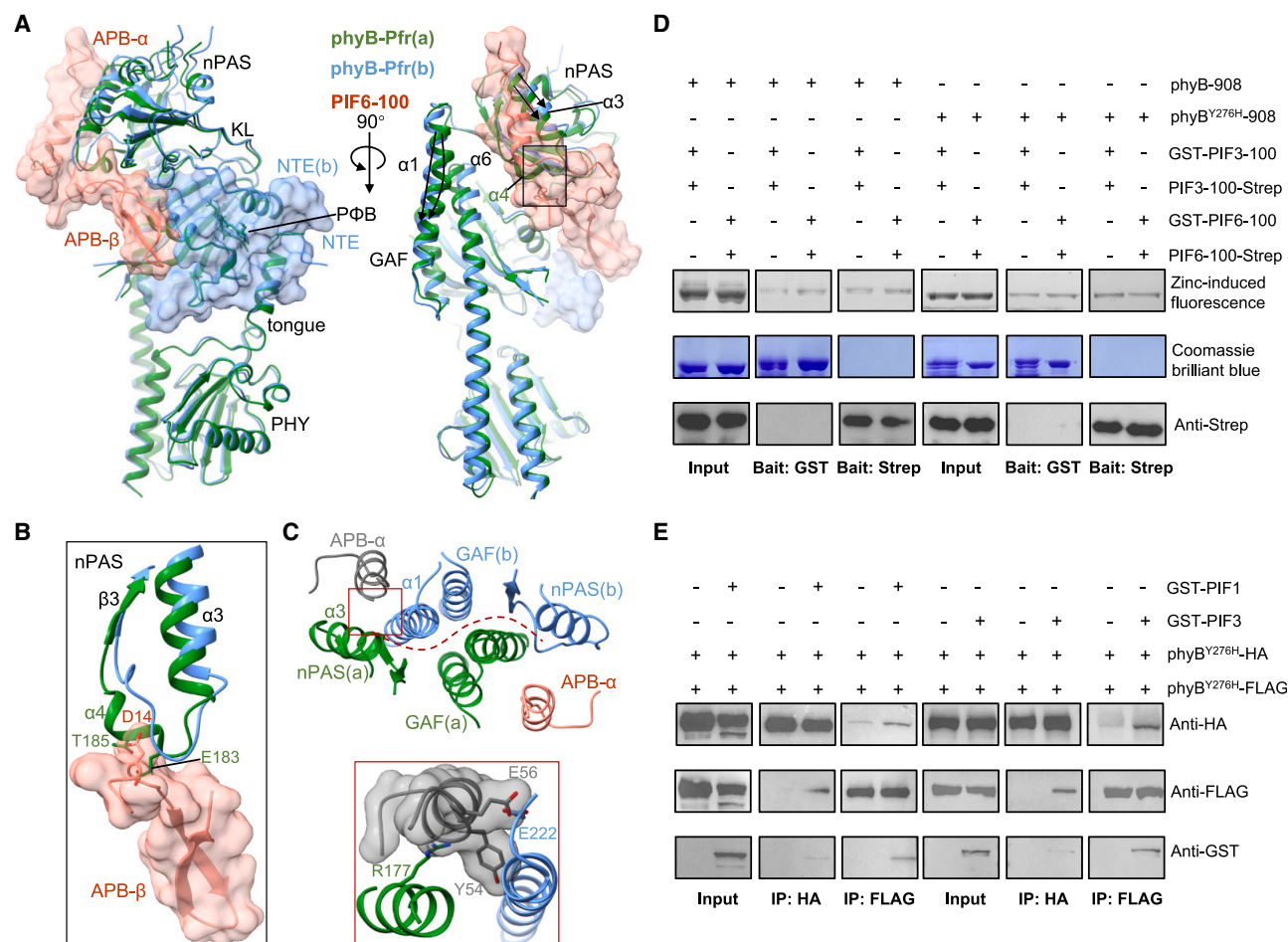
See also Figure S6 and Data S1.

Figure 7. The asymmetric phyB-Pfr dimer allows the binding of only one PIF6-100

(A) Structural comparison of PIF6-APB-β-bound phyB-Pfr (blue) and free phyB-Pfr (green), shown in two orientations. PIF6-100 (salmon) and phyB-NTE (blue), shown in surface. Arrows indicate the orientation of GAF-α1 or nPAS-α3.

(B) Details of clashes between the N-terminal loop of PIF6-APB-β (salmon) and the nPAS-α4 in phyB(a) (green), indicated by black box in (A).

(C) Top: alignment of PIF6-APB-α (gray) to the other side of dimerization interface. Bottom: details of clashes between PIF6-APB-α (gray) and the other side of dimerization interface (color-coded), indicated by salmon box in top.

(D) Equal amounts of GST- and strep-tagged PIF6-100 (or PIF3) were co-incubated with excessive phyB-908 under Rc (or phyB[Y276H]-908 under white light). Following pull-down by either of the tags and extensive washing, the beads were simultaneously analyzed by Coomassie brilliant blue staining for GST-tagged PIF6-100 (or PIF3) and immunoblot for strep-tagged PIF6-100 (or PIF3).

(E) Equal amounts of HA- and FLAG-tagged full-length phyB[Y276H] were co-incubated with or without excessive full-length PIF1 (or PIF3) under white light. After coIP using either of the tags and extensive washing, immunoblots were performed to detect these proteins.

See also Figures S7 and S8 and Data S2.

Asymmetric dimerization of phyB-Pfr results in a 2:1 stoichiometry of phyB and PIF6-100

Our structure unexpectedly reveals a 2:1 stoichiometry between phyB and PIF6-100. Structural comparison indicates that GAF-α1, GAF-α6, and the nPAS domain in phyB(a) have notably different conformations from their counterparts in phyB(b) (Figures 6A and 7A), thus resulting in an asymmetric dimer of the PIF6-100 bound phyB-Pfr. Helix-α4 of nPAS in phyB(a) substantially clashes with the N-terminal loop of PIF6-APB-β, while the helix refolds into a loop in the PIF6-APB-β-bound phyB(b) (Figures 7A, 7B, and S7A). Additionally, when the PIF6-APB-α is aligned to the opposite side of the phyB-Pfr dimerization interface, GAF-α1 in phyB(b) and nPAS-α3 in phyB(a) severely clash

with PIF6-APB-α (Figure 7C). Collectively, the structural differences in the asymmetric phyB dimer account for the 2:1 stoichiometry of the phyB-PIF6-100 complex.

Our biochemical data further demonstrated that when GST- and strep-tagged PIF6-100 were co-incubated with phyB-908 under red light, the strep-tagged PIF6-100 cannot be detected in the pull-down sample by GST-tagged PIF6-100, and vice versa (Figure 7D; Data S2). This result confirms that the two forms of PIF6-100 cannot coexist simultaneously with a phyB-Pfr dimer, thereby supporting the 2:1 ratio of phyB-Pfr to PIF6. Similar results were observed with PIF3-100 (Figure 7D; Data S2). Furthermore, only one form of PIF-100 was detected in the pull-down sample with phyB[Y276H]-908 (Figure 7D; Data S2). To

further assess the 2:1 phyB-PIF interaction, full-length PIF proteins were used in co-immunoprecipitation (coIP) assays. After co-incubating the HA- and FLAG-tagged phyB^{Y276H} proteins with GST-tagged PIF1 or PIF3, in the samples precipitated by anti-HA beads, the presence of full-length PIF resulted in a substantial increase in the detection of the FLAG-tagged phyB, whereas negligible levels were observed in the absence of PIF (Figure 7E; Data S2). Likewise, when anti-FLAG beads were used for coIP, a significant increase in the detection of the HA-tagged phyB was evident upon the addition of PIF1 or PIF3. These results suggest that the full-length dimeric PIF protein can simultaneously bind to two phyB dimers, supporting a 4:2 (2:1) stoichiometry. Additionally, increased detection of two types of phyB in the coIP samples with PIF was also observed in the protoplast assays (Figure S7B; Data S2). Altogether, our data indicate the existence of a 2:1 molar ratio of phyB-Pfr and PIF.

DISCUSSION

Photoactivation of phyB
Our structures reveal a head-to-head dimer of the photoactivated phyB-Pfr or constitutively active phyB^{Y276H} bound by PIF6-100, which is mediated by the N-terminal PSM. This finding is supported by biochemical and functional data. Compared with phyB-Pr,[42] our two PIF6-bound phyB structures reveal a cascade of structural remodelings during phyB photoactivation. Upon red light absorption, the PΦB molecule switches its configuration, accompanied by an exchange of new contacts between PΦB and its binding pocket. These events result in the transition of the PHY tongue in the N-terminal PSM of phyB. These structural observations remarkably resemble the "flip and slide" and "toggle" models that illustrate the conformational changes of the bilin chromophore and PHY tongue, respectively, in bacterial phys,[15,57] indicating a conserved mechanism of transducing light signal. Furthermore, our phyB^{Y276H} structure confirms that the conformation of PΦB-contacting residues and the α-helical PHY tongue match that of phyB-Pfr. By mimicking the conformation of Y276 in Pfr, H276 drives PΦB to a position similar to that in phyB-Pfr, thereby triggering subsequent conformational changes of other PΦB-contacting residues and the PHY tongue. These structural observations also explain why PΦB is required for phyB^{Y276H} to initiate phyB signaling, despite the absence of a light-induced configuration switch.[21,46]

The PHY tongue transition subsequently triggers a conformational change in the C-terminal HK domain for activation in bacterial Phys (Figure S3F).[39] In comparison, the α-helical PHY tongue is predicted to directly interfere with the Mod of PAS2 in phyB-Pr, thereby disrupting the head-to-tail PSM dimer stabilized by the C-terminal PAS2 and HKRD domains. As a result, phyB is fully activated by freeing the N-terminal PSM for PIF recognition. This agrees with the observation that the interactions between the N and C termini of phyB are disrupted in the Pfr state.[18,58] The Pfr form also exhibits greater flexibility and susceptibility to protease treatment than the Pr form.[58] Additionally, phyB-Pfr is shown to be dimeric (Figure 1A),[56] whereas the Pfr form of phyB-PSM, phyB-908, and phyB^{Y276H}-908 are mainly monomeric,[19,46,51] suggesting that the C terminus of phyB-Pfr

remains dimeric. It is plausible that phyB-Pfr alone exhibits high flexibility due to the distinct arrangements of its N and C termini.

Specific recognition of PIF by phyB-Pfr
PIF6 exhibits a high affinity and specificity for phyB-Pfr,[26] making it frequently exploited in optogenetics.[48,59–63] Our study reveals the specific recognition of PIF6 by phyB-Pfr through an induced-fit mechanism, which can be utilized to optimize the phyB-PIF light-switch tool for optogenetics. Based on our structures, PIF6-100 can be divided into two parts: the N-terminal PIF6-APB-β and C-terminal PIF6-APB-α. The recognition of these two parts of PIF6-100 is dependent on the phyB-NTE and a head-to-head dimer of phyB-PSM, respectively. However, the NTE is flexible and the PSM mainly exists as a monomer in phyB-Pfr, indicating an induced-fit recognition mechanism wherein PIF6-100 binding leads to the formation of a head-to-head dimer of phyB-Pfr with a stabilized NTE. This induced-fit mechanism could explain the versatile functionality and photo-reversibility of phyB. In addition to the PIFs, other components have been found to associate with photoactivated phyB.[5,64,65] The inherent flexibility of phyB-Pfr allows it to recognize various partners through an induced-fit mechanism. Furthermore, both the stabilized NTE and head-to-head dimer of phyB-Pfr, induced by PIF6-100 binding, effectively impede phyB dark reversion. Hence, the induced-fit mechanism favors the reversibility of phyB in the absence of a binding partner.

NTE is specific to plant Phys and has been shown to control dark reversion through phosphorylation in phyB signaling.[66–68] Our structures reveal that the PIF-APB-β-bound NTE can stabilize phyB-Pfr through contacts with PΦB and the α-helical PHY tongue, whereas the PHY tongue in phyB-Pr is predicted to prevent the NTE remodeling and PIF6-APB-β binding. Therefore, the light-induced transition of the PHY tongue is a prerequisite for recognition of both PIF6-APB-β and PIF6-APB-α by phyB-Pfr. Supporting our structural observations, the missense mutations S86E and Y104E in phyB-NTE, which accelerate dark reversion and impair PIF3 interaction *in vivo*,[66,67] destabilize NTE (Figure 5B). Moreover, our NTE structure reveals the exposure of residues S80 and S106, and the disordered nature of its very N terminus (Figure 5B; Data S2), rationalizing their respective roles in nuclear import of phyB and thermal sensing.[69–72]

The highly conserved APB-β in other PIFs likely binds to phyB in a similar manner to PIF6, as suggested by our and previous studies.[26,47] Additionally, phyB mutants with reduced ability to bind PIF6-APB-β impaired phyB function, likely due to the inability to control PIF1/3/4/5 signaling. Furthermore, three residues of phyB, namely R110, G112, and R352, have been demonstrated to participate in PIF3 binding.[73,74] These residues are located in the KL and its nearby NTE of phyB, coinciding with PIF6-APB-β-interacting elements. As for the less-conserved APB-α, our and previous studies demonstrate its contribution to phyB binding, resulting in varying affinities.[26,48] Considering that the N-terminal PSM dimerization is essential for phyB signaling,[19] it is reasonable to assume that the APB-α of other PIFs participates in phyB dimerization like PIF6-APB-α.

2:1 stoichiometry of phyB and PIF6-100

Previous *in vitro* studies have indicated a 1:1 stoichiometry for the phyB-PIF3 interaction.[75] However, an approximate 1:2 stoichiometry was observed between phyB and PIF4.[76] Interestingly, our cryo-EM structures reveal a 2:1 stoichiometry between phyB-Pfr or phyB[Y276H] and PIF6-100. This structural observation is further supported by biochemical data. The asymmetric phyB dimer stabilized by one PIF6-100 assumes a non-productive conformation to bind a second PIF6-100 molecule. Intriguingly, the crystal structure of the N-terminal PSM of phyB-Pr reveals a head-to-head dimer that closely resembles the PIF6-bound phyB-Pfr or phyB[Y276H] dimer (Figure S7C). Both structures share a similar asymmetric dimerization interface (Figures S7D and S7E). Nonetheless, the crystal structure of the nPAS-GAF segment of *Sorghum bicolor* phyB reveals a symmetric dimerization pattern (Figure S7F).[51] Therefore, whether the asymmetry in phyB-Pfr or phyB[Y276H] dimer is inherent or induced by PIF6-100 binding remains to be determined.

Then, what can be the potential significance of the unexpected stoichiometry between phyB and PIF6-100? Our data suggest that this may facilitate the photo-reversibility of phyB. A single PIF6-100 molecule stabilizes one NTE and binds to one side of the phyB-Pfr dimer, leaving the opposite side with a flexible NTE and an empty interface. This conformation facilitates the reversion of the PHY tongue and the C-terminal PAS2-HKRD to their Pr state. Given the spectral data illustrating the remarkable inhibition of phyB dark reversion by PIF6-100, we speculate that the binding of two PIF6 molecules might freeze phyB in the Pfr state, thereby blocking the reversibility of this photoreceptor. Alternatively, previous studies have indicated that phyB-Pfr can directly obstruct PIFs from binding promoter DNAs.[33,34] Our Alphafold2 predictions show that the full-length dimeric PIFs have a highly disordered nature (Figures S7G–S7I).[77] Intriguingly, the two individual PIF-APB motifs, adopting β-hairpin structures, are positioned close to the opposite side of the bHLH dimer, suggesting a potential mechanism whereby the binding of two phyB-Pfr dimers to each PIF-APB could cause steric hindrance with PIF-bHLH (Figure S7J), thereby impairing its DNA-binding activity. Additionally, recent reports indicate a transcription activation domain (TAD) proximal to PIF3-APB.[78,79] Thus, if PIF3-APB binds to a head-to-head phyB dimer like PIF6-100, the function of TAD could be influenced due to the limited space available for recruiting transcription-related components. It will be of interest to investigate whether other phyB-PIF interactions also possess a 2:1 stoichiometry.

In summary, our data support a model wherein the photoactivated phyB recognizes its PIF partner (Figure S8). The phyB-Pr assembles into a head-to-tail dimer. Light exposure triggers a configuration switch of PΦB, inducing the PHY tongue transition from a β-sheet to an α-helix. The resulting α-helical PHY tongue directly clashes with the Mod of PAS2, destabilizing the phyB-Pr dimer mediated by the PAS2-HKRD module. These structural remodelings of phyB enable the binding of APB-β and APB-α in PIF6-100, which consequently stabilize the NTE and a head-to-head dimer of phyB-Pfr by an induced-fit mechanism, culminating in the assembly of a phyB-PIF signaling complex.

Limitations of the study

In this study, we reported the structures of the photoactivated phyB-Pfr or the widely employed active mutant phyB[Y276H], both in complex with PIF6-100, revealing the activation of a plant phy by light and its subsequent interaction with a PIF signaling partner. However, two key questions warrant further investigation. First, our gel filtration assays indicate the presence of a small fraction of phyB[Y276H]-908 or phyB-908-Pfr dimers, suggesting the possibility of solving a structure of phyB-Pfr alone. This would elucidate whether the asymmetry in the phyB-Pfr dimer is intrinsic or induced by PIF6-100. Second, an unexpected 2:1 stoichiometry between phyB and PIF6-100 was observed in both structures, a finding corroborated *in vitro* and in the *Arabidopsis* protoplast. However, additional research is required to ascertain how this interaction mechanism impacts the DNA-binding activity of full-length PIF6 and whether it is conserved across the PIF family.

DECLARATION OF INTERESTS

The authors declare no competing interests.

STAR★METHODS

Detailed methods are provided in the online version of this paper and include the following:

- KEY RESOURCES TABLE
- EXPERIMENTAL MODEL AND SUBJECT DETAILS
  - Bacterial strains
  - Insect cell lines
  - Plant materials and growth conditions
- METHOD DETAILS
  - Recombinant protein expression and purification
  - Reconstitution of the phyB-PIF6 complexes
  - Gel filtration assays
  - Cryo-EM sample preparation and data collection
  - Cryo-EM data processing
  - Model building and refinement
  - *in vitro* Pull-down assays
  - Co-Immunoprecipitation (CoIP) assays
  - Immunoblot assays
  - Subcellular fluorescence imaging
  - UV-vis absorption spectroscopy and kinetics of dark reversion
- QUANTIFICATION AND STATISTICAL ANALYSIS

SUPPLEMENTAL INFORMATION

Supplemental information can be found online at https://doi.org/10.1016/j.cell.2024.09.005.

REFERENCES

1. Paik, I., and Huq, E. (2019). Plant photoreceptors: multi-functional sensory proteins and their signaling networks. Semin. Cell Dev. Biol. *92*, 114–121. https://doi.org/10.1016/j.semcdb.2019.03.007.

2. Rockwell, N.C., and Lagarias, J.C. (2020). Phytochrome evolution in 3D: deletion, duplication, and diversification. New Phytol. *225*, 2283–2300. https://doi.org/10.1111/nph.16240.

3. Hughes, J., and Winkler, A. (2024). New insight into phytochromes: connecting structure to function. Annu. Rev. Plant Biol. *75*, 153–183. https://doi.org/10.1146/annurev-arplant-070623-110636.

4. Rockwell, N.C., Su, Y.S., and Lagarias, J.C. (2006). Phytochrome structure and signaling mechanisms. Annu. Rev. Plant Biol. *57*, 837–858. https://doi.org/10.1146/annurev.arplant.56.032604.144208.

5. Bae, G., and Choi, G. (2008). Decoding of light signals by plant phytochromes and their interacting proteins. Annu. Rev. Plant Biol. *59*, 281–311. https://doi.org/10.1146/annurev.arplant.59.032607.092859.

6. Li, J., Li, G., Wang, H., and Wang Deng, X. (2011). Phytochrome signaling mechanisms. Arabidopsis Book *9*, e0148. https://doi.org/10.1199/tab.0148.

7. Legris, M., Ince, Y.Ç., and Fankhauser, C. (2019). Molecular mechanisms underlying phytochrome-controlled morphogenesis in plants. Nat. Commun. *10*, 5219. https://doi.org/10.1038/s41467-019-13045-0.

8. Leivar, P., and Quail, P.H. (2011). PIFs: pivotal components in a cellular signaling hub. Trends Plant Sci. *16*, 19–28. https://doi.org/10.1016/j.tplants.2010.08.003.

9. Pham, V.N., Kathare, P.K., and Huq, E. (2018). Phytochromes and phytochrome interacting factors. Plant Physiol. *176*, 1025–1038. https://doi.org/10.1104/pp.17.01384.

10. Ushijima, T., Hanada, K., Gotoh, E., Yamori, W., Kodama, Y., Tanaka, H., Kusano, M., Fukushima, A., Tokizawa, M., Yamamoto, Y.Y., et al. (2017). Light controls protein localization through phytochrome-mediated alternative promoter selection. Cell *171*, 1316–1325.e12. https://doi.org/10.1016/j.cell.2017.10.018.

11. Li, F.W., Melkonian, M., Rothfels, C.J., Villarreal, J.C., Stevenson, D.W., Graham, S.W., Wong, G.K.S., Pryer, K.M., and Mathews, S. (2015). Phytochrome diversity in green plants and the origin of canonical plant phytochromes. Nat. Commun. *6*, 7852. https://doi.org/10.1038/ncomms8852.

12. Chen, M., and Chory, J. (2011). Phytochrome signaling mechanisms and the control of plant development. Trends Cell Biol. *21*, 664–671. https://doi.org/10.1016/j.tcb.2011.07.002.

13. Xu, X., Paik, I., Zhu, L., and Huq, E. (2015). Illuminating progress in phytochrome-mediated light signaling pathways. Trends Plant Sci. *20*, 641–650. https://doi.org/10.1016/j.tplants.2015.06.010.

14. Cheng, M.C., Kathare, P.K., Paik, I., and Huq, E. (2021). Phytochrome signaling networks. Annu. Rev. Plant Biol. *72*, 217–244. https://doi.org/10.1146/annurev-arplant-080620-024221.

15. Burgie, E.S., and Vierstra, R.D. (2014). Phytochromes: an atomic perspective on photoactivation and signaling. Plant Cell *26*, 4568–4583. https://doi.org/10.1105/tpc.114.131623.

16. Wagner, J.R., Brunzelle, J.S., Forest, K.T., and Vierstra, R.D. (2005). A light-sensing knot revealed by the structure of the chromophore-binding domain of phytochrome. Nature *438*, 325–331. https://doi.org/10.1038/nature04118.

17. Chen, M., Schwab, R., and Chory, J. (2003). Characterization of the requirements for localization of phytochrome B to nuclear bodies. Proc. Natl. Acad. Sci. USA *100*, 14493–14498. https://doi.org/10.1073/pnas.1935989100.

18. Chen, M., Tao, Y., Lim, J., Shaw, A., and Chory, J. (2005). Regulation of phytochrome B nuclear localization through light-dependent unmasking of nuclear-localization signals. Curr. Biol. *15*, 637–642. https://doi.org/10.1016/j.cub.2005.02.028.

19. Matsushita, T., Mochizuki, N., and Nagatani, A. (2003). Dimers of the N-terminal domain of phytochrome B are functional in the nucleus. Nature *424*, 571–574. https://doi.org/10.1038/nature01837.

20. Qiu, Y.J., Pasoreck, E.K., Reddy, A.K., Nagatani, A., Ma, W.X., Chory, J., and Chen, M. (2017). Mechanism of early light signaling by the carboxy-terminal output module of phytochrome B. Nat. Commun. *8*, 1905. https://doi.org/10.1038/s41467-017-02062-6.

21. Su, Y.S., and Lagarias, J.C. (2007). Light-independent phytochrome signaling mediated by dominant GAF domain tyrosine mutants of phytochromes in transgenic plants. Plant Cell *19*, 2693–2694. https://doi.org/10.1105/tpc.107.190862.

22. Ni, M., Tepperman, J.M., and Quail, P.H. (1998). PIF3, a phytochrome-interacting factor necessary for normal photoinduced signal transduction, is a novel basic helix-loop-helix protein. Cell *95*, 657–667. https://doi.org/10.1016/s0092-8674(00)81636-0.

23. Huq, E., Al-Sady, B., Hudson, M., Kim, C., Apel, K., and Quail, P.H. (2004). Phytochrome-interacting factor 1 is a critical bHLH regulator of chlorophyll biosynthesis. Science *305*, 1937–1941. https://doi.org/10.1126/science.1099728.

24. Lee, N., and Choi, G. (2017). Phytochrome-interacting factor from Arabidopsis to liverwort. Curr. Opin. Plant Biol. *35*, 54–60. https://doi.org/10.1016/j.pbi.2016.11.004.

25. Martínez-García, J.F., Huq, E., and Quail, P.H. (2000). Direct targeting of light signals to a promoter element-bound transcription factor. Science *288*, 859–863. https://doi.org/10.1126/science.288.5467.859.

26. Khanna, R., Huq, E., Kikis, E.A., Al-Sady, B., Lanzatella, C., and Quail, P.H. (2004). A novel molecular recognition motif necessary for targeting

photoactivated phytochrome signaling to specific basic helix-loop-helix transcription factors. Plant Cell *16*, 3033–3044. https://doi.org/10.1105/tpc.104.025643.

27. Leivar, P., Monte, E., Oka, Y., Liu, T., Carle, C., Castillon, A., Huq, E., and Quail, P.H. (2008). Multiple phytochrome-interacting bHLH transcription factors repress premature seedling photomorphogenesis in darkness. Curr. Biol. *18*, 1815–1823. https://doi.org/10.1016/j.cub.2008.10.058.

28. Leivar, P., Tepperman, J.M., Monte, E., Calderon, R.H., Liu, T.L., and Quail, P.H. (2009). Definition of early transcriptional circuitry involved in light-induced reversal of PIF-imposed repression of photomorphogenesis in young seedlings. Plant Cell *21*, 3535–3553. https://doi.org/10.1105/tpc.109.070672.

29. Shin, J., Kim, K., Kang, H., Zulfugarov, I.S., Bae, G., Lee, C.H., Lee, D., and Choi, G. (2009). Phytochromes promote seedling light responses by inhibiting four negatively-acting phytochrome-interacting factors. Proc. Natl. Acad. Sci. USA *106*, 7660–7665. https://doi.org/10.1073/pnas.0812219106.

30. Bauer, D., Viczián, A., Kircher, S., Nobis, T., Nitschke, R., Kunkel, T., Panigrahi, K.C.S., Adám, E., Fejes, E., Schäfer, E., and Nagy, F. (2004). Constitutive photomorphogenesis 1 and multiple photoreceptors control degradation of phytochrome interacting factor 3, a transcription factor required for light signaling in Arabidopsis. Plant Cell *16*, 1433–1445. https://doi.org/10.1105/tpc.021568.

31. Ni, W.M., Xu, S.L., Tepperman, J.M., Stanley, D.J., Maltby, D.A., Gross, J.D., Burlingame, A.L., Wang, Z.Y., and Quail, P.H. (2014). A mutually assured destruction mechanism attenuates light signaling in Arabidopsis. Science *344*, 1160–1164. https://doi.org/10.1126/science.1250778.

32. Ni, W.M., Xu, S.L., González-Grandío, E., Chalkley, R.J., Huhmer, A.F.R., Burlingame, A.L., Wang, Z.Y., and Quail, P.H. (2017). PPKs mediate direct signal transfer from phytochrome photoreceptors to transcription factor PIF3. Nat. Commun. *8*, 15236. https://doi.org/10.1038/ncomms15236.

33. Park, E., Park, J., Kim, J., Nagatani, A., Lagarias, J.C., and Choi, G. (2012). Phytochrome B inhibits binding of phytochrome-interacting factors to their target promoters. Plant J. *72*, 537–546. https://doi.org/10.1111/j.1365-313X.2012.05114.x.

34. Park, E., Kim, Y., and Choi, G. (2018). Phytochrome B requires PIF degradation and sequestration to induce light responses across a wide range of light conditions. Plant Cell *30*, 1277–1292. https://doi.org/10.1105/tpc.17.00913.

35. Takala, H., Björling, A., Berntsson, O., Lehtivuori, H., Niebling, S., Hoernke, M., Kosheleva, I., Henning, R., Menzel, A., Ihalainen, J.A., and Westenhoff, S. (2014). Signal amplification and transduction in phytochrome photosensors. Nature *509*, 245–248. https://doi.org/10.1038/nature13310.

36. Burgie, E.S., Zhang, J., and Vierstra, R.D. (2016). Crystal structure of Deinococcus phytochrome in the photoactivated state reveals a cascade of structural rearrangements during photoconversion. Structure *24*, 448–457. https://doi.org/10.1016/j.str.2016.01.001.

37. Gourinchas, G., Heintz, U., and Winkler, A. (2018). Asymmetric activation mechanism of a homodimeric red light-regulated photoreceptor. eLife *7*, e34815. https://doi.org/10.7554/eLife.34815.

38. Otero, L.H., Foscaldi, S., Antelo, G.T., Rosano, G.L., Sirigu, S., Klinke, S., Defelipe, L.A., Sánchez-Lamas, M., Battocchio, G., Conforte, V., et al. (2021). Structural basis for the Pr-Pfr long-range signaling mechanism of a full-length bacterial phytochrome at the atomic level. Sci. Adv. *7*, eabh1097. https://doi.org/10.1126/sciadv.abh1097.

39. Wahlgren, W.Y., Claesson, E., Tuure, I., Trillo-Muyo, S., Bódizs, S., Ihalainen, J.A., Takala, H., and Westenhoff, S. (2022). Structural mechanism of signal transduction in a phytochrome histidine kinase. Nat. Commun. *13*, 7673. https://doi.org/10.1038/s41467-022-34893-3.

40. Gourinchas, G., Etzl, S., Göbl, C., Vide, U., Madl, T., and Winkler, A. (2017). Long-range allosteric signaling in red light-regulated diguanylyl cyclases. Sci. Adv. *3*, e1602498. https://doi.org/10.1126/sciadv.1602498.

41. Krall, L., and Reed, J.W. (2000). The histidine kinase-related domain participates in phytochrome B function but is dispensable. Proc. Natl. Acad. Sci. USA *97*, 8169–8174. https://doi.org/10.1073/pnas.140520097.

42. Li, H., Burgie, E.S., Gannam, Z.T.K., Li, H.L., and Vierstra, R.D. (2022). Plant phytochrome B is an asymmetric dimer with unique signalling potential. Nature *604*, 127–133. https://doi.org/10.1038/s41586-022-04529-z.

43. Burgie, E.S., Li, H., Gannam, Z.T.K., McLoughlin, K.E., Vierstra, R.D., and Li, H.L. (2023). The structure of phytochrome A reveals topological and functional diversification among the plant photoreceptor isoforms. Nat. Plants *9*, 1116–1129. https://doi.org/10.1038/s41477-023-01435-8.

44. Wang, J., Zhou, C., Guan, Z.Y., Wang, Q., Zhao, J., Wang, L.X., Zhang, L.Q., Zhang, D.L., Deng, X.W., Ma, L., and Yin, P. (2023). Plant phytochrome A in the Pr state assembles as an asymmetric dimer. Cell Res. *33*, 802–805. https://doi.org/10.1038/s41422-023-00847-7.

45. Zhang, Y.X., Lin, X.L., Ma, C.Y., Zhao, J., Shang, X.J., Wang, Z.D., Xu, B., Gao, N., Deng, X.W., and Wang, J.Z. (2023). Structural insights into plant phytochrome A as a highly sensitized photoreceptor. Cell Res. *33*, 806–809. https://doi.org/10.1038/s41422-023-00858-4.

46. Burgie, E.S., Bussell, A.N., Walker, J.M., Dubiel, K., and Vierstra, R.D. (2014). Crystal structure of the photosensing module from a red/far-red light-absorbing plant phytochrome. Proc. Natl. Acad. Sci. USA *111*, 10179–10184. https://doi.org/10.1073/pnas.1403096111.

47. Shen, H., Zhu, L., Castillon, A., Majee, M., Downie, B., and Huq, E. (2008). Light-induced phosphorylation and degradation of the negative regulator PHYTOCHROME-INTERACTING FACTOR1 from Arabidopsis depend upon its direct physical interactions with photoactivated phytochromes. Plant Cell *20*, 1586–1602. https://doi.org/10.1105/tpc.108.060020.

48. Golonka, D., Fischbach, P., Jena, S.G., Kleeberg, J.R.W., Essen, L.O., Toettcher, J.E., Zurbriggen, M.D., and Möglich, A. (2019). Deconstructing and repurposing the light-regulated interplay between phytochromes and interacting factors. Commun. Biol. *2*, 448. https://doi.org/10.1038/s42003-019-0687-9.

49. Essen, L.O., Mailliet, J., and Hughes, J. (2008). The structure of a complete phytochrome sensory module in the Pr ground state. Proc. Natl. Acad. Sci. USA *105*, 14709–14714. https://doi.org/10.1073/pnas.0806477105.

50. Yang, X., Kuk, J., and Moffat, K. (2008). Crystal structure of Pseudomonas aeruginosa bacteriophytochrome: photoconversion and signal transduction. Proc. Natl. Acad. Sci. USA *105*, 14715–14720. https://doi.org/10.1073/pnas.0806718105.

51. Nagano, S., Guan, K.L., Shenkutie, S.M., Feiler, C., Weiss, M., Kraskov, A., Buhrke, D., Hildebrandt, P., and Hughes, J. (2020). Structural insights into photoactivation and signalling in plant phytochromes. Nat. Plants *6*, 581–588. https://doi.org/10.1038/s41477-020-0638-y.

52. Ni, M., Tepperman, J.M., and Quail, P.H. (1999). Binding of phytochrome B to its nuclear signalling partner PIF3 is reversibly induced by light. Nature *400*, 781–784. https://doi.org/10.1038/23500.

53. Shimizu-Sato, S., Huq, E., Tepperman, J.M., and Quail, P.H. (2002). A light-switchable gene promoter system. Nat. Biotechnol. *20*, 1041–1044. https://doi.org/10.1038/nbt734.

54. Burgie, E.S., Bussell, A.N., Lye, S.H., Wang, T., Hu, W.M., McLoughlin, K.E., Weber, E.L., Li, H.L., and Vierstra, R.D. (2017). Photosensing and thermosensing by phytochrome B require both proximal and distal allosteric features within the dimeric photoreceptor. Sci. Rep. *7*, 13648. https://doi.org/10.1038/s41598-017-14037-0.

55. Burgie, E.S., Gannam, Z.T.K., McLoughlin, K.E., Sherman, C.D., Holehouse, A.S., Stankey, R.J., and Vierstra, R.D. (2021). Differing biophysical properties underpin the unique signaling potentials within the plant phytochrome photoreceptor families. Proc. Natl. Acad. Sci. USA *118*, e2105649118. https://doi.org/10.1073/pnas.2105649118.

56. Klose, C., Venezia, F., Hussong, A., Kircher, S., Schäfer, E., and Fleck, C. (2015). Systematic analysis of how phytochrome B dimerization determines its specificity. Nat. Plants *1*, 15090. https://doi.org/10.1038/Nplants.2015.90.

57. Yang, X.J., Kuk, J., and Moffat, K. (2009). Conformational differences between the Pfr and Pr states in bacteriophytochrome. Proc. Natl. Acad. Sci. USA *106*, 15639–15644. https://doi.org/10.1073/pnas.0902178106.

58. Park, C.M., Bhoo, S.H., and Song, P.S. (2000). Inter-domain crosstalk in the phytochrome molecules. Semin. Cell Dev. Biol. *11*, 449–456. https://doi.org/10.1006/scdb.2000.0200.

59. Levskaya, A., Weiner, O.D., Lim, W.A., and Voigt, C.A. (2009). Spatiotemporal control of cell signalling using a light-switchable protein interaction. Nature *461*, 997–1001. https://doi.org/10.1038/nature08446.

60. Toettcher, J.E., Gong, D., Lim, W.A., and Weiner, O.D. (2011). Light-based feedback for controlling intracellular signaling dynamics. Nat. Methods *8*, 837–839. https://doi.org/10.1038/Nmeth.1700.

61. Müller, K., Zurbriggen, M.D., and Weber, W. (2014). Control of gene expression using a red- and far-red light–responsive bi-stable toggle switch. Nat. Protoc. *9*, 622–632. https://doi.org/10.1038/nprot.2014.038.

62. Ochoa-Fernandez, R., Abel, N.B., Wieland, F.G., Schlegel, J., Koch, L.A., Miller, J.B., Engesser, R., Giuriani, G., Brandl, S.M., Timmer, J., et al. (2020). Optogenetic control of gene expression in plants in the presence of ambient white light. Nat. Methods *17*, 717–725. https://doi.org/10.1038/s41592-020-0868-y.

63. Konrad, K.R., Gao, S., Zurbriggen, M.D., and Nagel, G. (2023). Optogenetic methods in plant biology. Annu. Rev. Plant Biol. *74*, 313–339. https://doi.org/10.1146/annurev-arplant-071122-094840.

64. Ryu, J.S., Kim, J.I., Kunkel, T., Kim, B.C., Cho, D.S., Hong, S.H., Kim, S.H., Fernández, A.P., Kim, Y., Alonso, J.M., et al. (2005). Phytochrome-specific type 5 phosphatase controls light signal flux by enhancing phytochrome stability and affinity for a signal transducer. Cell *120*, 395–406. https://doi.org/10.1016/j.cell.2004.12.019.

65. Chen, M., Galvão, R.M., Li, M.N., Burger, B., Bugea, J., Bolado, J., and Chory, J. (2010). Arabidopsis HEMERA/pTAC12 initiates photomorphogenesis by phytochromes. Cell *141*, 1230–1240. https://doi.org/10.1016/j.cell.2010.05.007.

66. Medzihradszky, M., Bindics, J., Ádám, É., Viczián, A., Klement, É., Lorrain, S., Gyula, P., Mérai, Z., Fankhauser, C., Medzihradszky, K.F., et al. (2013). Phosphorylation of phytochrome B inhibits light-induced signaling via accelerated dark reversion in Arabidopsis. Plant Cell *25*, 535–544. https://doi.org/10.1105/tpc.112.106898.

67. Nito, K., Wong, C.C.L., Yates, J.R., and Chory, J. (2013). Tyrosine phosphorylation regulates the activity of phytochrome photoreceptors. Cell Rep. *3*, 1970–1979. https://doi.org/10.1016/j.celrep.2013.05.006.

68. Viczián, A., Ádám, É., Staudt, A.M., Lambert, D., Klement, E., Romero Montepaone, S.R., Hiltbrunner, A., Casal, J., Schäfer, E., Nagy, F., and Klose, C. (2020). Differential phosphorylation of the N-terminal extension regulates phytochrome B signaling. New Phytol. *225*, 1635–1650. https://doi.org/10.1111/nph.16243.

69. Jung, J.H., Domijan, M., Klose, C., Biswas, S., Ezer, D., Gao, M.J., Khattak, A.K., Box, M.S., Charoensawan, V., Cortijo, S., et al. (2016). Phytochromes function as thermosensors in Arabidopsis. Science *354*, 886–889. https://doi.org/10.1126/science.aaf6005.

70. Legris, M., Klose, C., Burgie, E.S., Rojas, C.C.R., Neme, M., Hiltbrunner, A., Wigge, P.A., Schäfer, E., Vierstra, R.D., and Casal, J.J. (2016). Phytochrome B integrates light and temperature signals in Arabidopsis. Science *354*, 897–900. https://doi.org/10.1126/science.aaf5656.

71. Chen, D., Lyu, M., Kou, X.X., Li, J., Yang, Z.X., Gao, L.L., Li, Y., Fan, L.M., Shi, H., and Zhong, S.W. (2022). Integration of light and temperature sensing by liquid-liquid phase separation of phytochrome B. Mol. Cell *82*, 3015–3029.e6. https://doi.org/10.1016/j.molcel.2022.05.026.

72. Zhao, Y., Shi, H., Pan, Y., Lyu, M., Yang, Z.X., Kou, X.X., Deng, X.W., and Zhong, S.W. (2023). Sensory circuitry controls cytosolic calcium-mediated phytochrome B phototransduction. Cell *186*, 1230–1243.e14. https://doi.org/10.1016/j.cell.2023.02.011.

73. Oka, Y., Matsushita, T., Mochizuki, N., Quail, P.H., and Nagatani, A. (2008). Mutant screen distinguishes between residues necessary for light-signal perception and signal transfer by phytochrome B. PLoS Genet. *4*, e1000158. https://doi.org/10.1371/journal.pgen.1000158.

74. Kikis, E.A., Oka, Y., Hudson, M.E., Nagatani, A., and Quail, P.H. (2009). Residues clustered in the light-sensing knot of phytochrome B are necessary for conformer-specific binding to signaling partner PIF3. PLoS Genet. *5*, e1000352. https://doi.org/10.1371/journal.pgen.1000352.

75. Zhu, Y.X., Tepperman, J.M., Fairchild, C.D., and Quail, P.H. (2000). Phytochrome B binds with greater apparent affinity than phytochrome A to the basic helix-loop-helix factor PIF3 in a reaction requiring the PAS domain of PIF3. Proc. Natl. Acad. Sci. USA *97*, 13419–13424. https://doi.org/10.1073/pnas.230433797.

76. Huq, E., and Quail, P.H. (2002). PIF4, a phytochrome-interacting bHLH factor, functions as a negative regulator of phytochrome B signaling in Arabidopsis. EMBO J. *21*, 2441–2450. https://doi.org/10.1093/emboj/21.10.2441.

77. Jumper, J., Evans, R., Pritzel, A., Green, T., Figurnov, M., Ronneberger, O., Tunyasuvunakool, K., Bates, R., Zídek, A., Potapenko, A., et al. (2021). Highly accurate protein structure prediction with AlphaFold. Nature *596*, 583–589. https://doi.org/10.1038/s41586-021-03819-2.

78. Dalton, J.C., Bätz, U., Liu, J., Curie, G.L., and Quail, P.H. (2016). A modified reverse one-hybrid screen identifies transcriptional activation domains in PHYTOCHROME-INTERACTING FACTOR 3. Front. Plant Sci. *7*, 881. https://doi.org/10.3389/fpls.2016.00881.

79. Yoo, C.Y., He, J.M., Sang, Q., Qiu, Y.J., Long, L.Y., Kim, R.J.A., Chong, E.G., Hahm, J., Morffy, N., Zhou, P., et al. (2021). Direct photoresponsive inhibition of a p53-like transcription activation domain in PIF3 by phytochrome B. Nat. Commun. *12*, 5614. https://doi.org/10.1038/s41467-021-25909-5.

80. Punjani, A., Rubinstein, J.L., Fleet, D.J., and Brubaker, M.A. (2017). cryoSPARC: algorithms for rapid unsupervised cryo-EM structure determination. Nat. Methods *14*, 290–296. https://doi.org/10.1038/Nmeth.4169.

81. Zivanov, J., Nakane, T., Forsberg, B.O., Kimanius, D., Hagen, W.J.H., Lindahl, E., and Scheres, S.H.W. (2018). New tools for automated high-resolution cryo-EM structure determination in RELION-3. eLife *7*, e42166. https://doi.org/10.7554/eLife.42166.

82. Meng, E.C., Goddard, T.D., Pettersen, E.F., Couch, G.S., Pearson, Z.J., Morris, J.H., and Ferrin, T.E. (2023). UCSF ChimeraX: Tools for structure building and analysis. Protein Sci. *32*, e4792. https://doi.org/10.1002/pro.4792.

83. Emsley, P., and Cowtan, K. (2004). COOT: model-building tools for molecular graphics. Acta Crystallogr. D Biol. Crystallogr. *60*, 2126–2132. https://doi.org/10.1107/S0907444904019158.

84. Liebschner, D., Afonine, P.V., Baker, M.L., Bunkóczi, G., Chen, V.B., Croll, T.I., Hintze, B., Hung, L.W., Jain, S., McCoy, A.J., et al. (2019). Macromolecular structure determination using X-rays, neutrons and electrons: recent developments in Phenix. Acta Crystallogr. D Struct. Biol. *75*, 861–877. https://doi.org/10.1107/S2059798319011471.

85. Robert, X., and Gouet, P. (2014). Deciphering key features in protein structures with the new ENDscript server. Nucleic Acids Res. *42*, W320–W324. https://doi.org/10.1093/nar/gku316.

86. Ni, W., Xu, S.L., Chalkley, R.J., Pham, T.N.D., Guan, S., Maltby, D.A., Burlingame, A.L., Wang, Z.Y., and Quail, P.H. (2013). Multisite light-induced phosphorylation of the transcription factor PIF3 is necessary for both its rapid degradation and concomitant negative feedback modulation of photoreceptor phyB levels in Arabidopsis. Plant Cell *25*, 2679–2698. https://doi.org/10.1105/tpc.113.112342.

STAR★METHODS

KEY RESOURCES TABLE

REAGENT or RESOURCE	SOURCE	IDENTIFIER
Antibodies		
Anti-GFP	EASYBIO	Cat#BE2002-100
Anti-Actin	EASYBIO	Cat#BE0028
Anti-Strep Tag II mouse monoclonal antibody	Sangon Biotech	Cat#D191106-0100
Anti-HA	Abmart	Cat#M20013; RRID: AB_2936242
Anti-FLAG	Sigma-Aldrich	Cat#F3165; RRID: AB_259529
Anti-GST	Abcam	Cat#ab19256; RRID: AB_444809
Anti-Myc	Sigma-Aldrich	Cat#M4439; RRID: AB_439694
Bacterial and virus strains		
E. coli DH5α competent cell	Lab stock	N/A
E. coli BL21 (DE3) competent cell	Lab stock	N/A
E. coli DH10Bac competent cell	Lab stock	N/A
Chemicals, peptides, and recombinant proteins		
Ni Sepharose 6 fast flow (Ni^{2+} resin)	Cytiva	Cat#17531802
Glutathione Sepharose™ 4B (GS4B resin)	Cytiva	Cat#17075604
Strep-Tactin®XT resin (Strep resin)	Cytiva	Cat#29401324
Anti-HA Affinity Beads	Smart-Lifesciences	Cat#SA068005
Anti-FLAG Affinity Beads	Smart-Lifesciences	Cat#SA042005
5-aminolevulinic acid (5-ALA)	Sigma-Aldrich	Cat#A3758
Critical commercial assays		
QIAGEN Plasmid Mini Kit (100)	QIAGEN	Cat#12125
TNT® SP6 Wheat Germ Expression System	Promega	Cat#L3261
Deposited data		
Cryo-EM map of phyB-Pfr-PIF6 complex	This paper	EMDB: EMD-39108
Model of phyB-Pfr-PIF6 complex	This paper	PDB: 8YB4
Cryo-EM map of phyB^{Y276H}-908-PIF6 complex	This paper	EMDB: EMD-60916
Model of phyB^{Y276H}-908-PIF6 complex	This paper	PDB: 9IUZ
Experimental models: Cell lines		
Spodoptera frugiperda (Sf21)	Lab stock	N/A
Experimental models: Organisms/strains		
Arabidopsis phyB-9	ABRC	N/A
Arabidopsis pPHYB:phyB-GFP/phyB-9	This paper	N/A
Arabidopsis pPHYB:phyB^{Y83W}-GFP/phyB-9	This paper	N/A
Arabidopsis pPHYB:phyB^{I101E}-GFP/phyB-9	This paper	N/A
Arabidopsis pPHYB:phyB$^{Q109A/R110A}$-GFP/phyB-9	This paper	N/A
Arabidopsis pPHYB:phyB^{L226Y}-GFP/phyB-9	This paper	N/A
Arabidopsis pPHYB:phyB^{F314A}-GFP/phyB-9	This paper	N/A
Arabidopsis pPHYB:phyB^{S584E}-GFP/phyB-9	This paper	N/A
Arabidopsis pPHYB:phyB^{I228E}-GFP/phyB-9	This paper	N/A
Arabidopsis pPHYB:phyB^{F420E}-GFP/phyB-9	This paper	N/A
Oligonucleotides		
Primers are listed in Table S3	This paper	N/A

(Continued on next page)

Continued

REAGENT or RESOURCE	SOURCE	IDENTIFIER
Recombinant DNA		
pFastBac-SUMO-phyB	This paper	N/A
pFastBac-SUMO-phyB^{Y276H}	This paper	N/A
pFastBac-SUMO-phyB^{Y276H}-HA	This paper	N/A
pFastBac-SUMO-phyB^{Y276H}-FLAG	This paper	N/A
pFastBac-SUMO-phyB-908	This paper	N/A
pFastBac-SUMO-phyB^{Y276H}-908	This paper	N/A
pFastBac-SUMO-phyB (111-1172) (ΔNTE)	This paper	N/A
pFastBac-SUMO-phyB^{G78A}	This paper	N/A
pFastBac-SUMO-phyB^{D82G}	This paper	N/A
pFastBac-SUMO-phyB^{Y83W}	This paper	N/A
pFastBac-SUMO-phyB^{I101E}	This paper	N/A
pFastBac-SUMO-phyB$^{Q109A/R110A}$	This paper	N/A
pFastBac-SUMO-phyB^{L226Y}	This paper	N/A
pFastBac-SUMO-phyB^{I228E}	This paper	N/A
pFastBac-SUMO-phyB^{Q310W}	This paper	N/A
pFastBac-SUMO-phyB^{F314A}	This paper	N/A
pFastBac-SUMO-phyB^{Q318A}	This paper	N/A
pFastBac-SUMO-phyB^{F420E}	This paper	N/A
pFastBac-SUMO-phyB^{S584E}	This paper	N/A
pFastBac-SUMO-phyB^{S584A}	This paper	N/A
pFastBac-SUMO-phyB^{S584K}	This paper	N/A
pFastBac-SUMO-phyB^{I855E}	This paper	N/A
pFastBac-SUMO-phyB-621	This paper	N/A
pET21b-SUMO-phyB (90-621)	This paper	N/A
pGEX-6P-1-PIF1-100	This paper	N/A
pGEX-6P-1-PIF3-100	This paper	N/A
pGEX-6P-1-PIF4-100	This paper	N/A
pGEX-6P-1-PIF7-100	This paper	N/A
pGEX-6P-1-PIF4 (1-43)	This paper	N/A
pGEX-6P-1-PIF3-100-Strep	This paper	N/A
pGEX-6P-1-PIF3-100^{E31A}	This paper	N/A
pGEX-6P-1-PIF3-100^{L32S}	This paper	N/A
pGEX-6P-1-PIF3-100^{W34A}	This paper	N/A
pGEX-6P-1-PIF3-100^{G37A}	This paper	N/A
pGEX-6P-1-PIF3-100^{I39S}	This paper	N/A
pGEX-6P-1-PIF3-100^{Q44A}	This paper	N/A
pGEX-6P-1-PIF6-100	This paper	N/A
pGEX-6P-1-PIF6 (1-37)	This paper	N/A
pGEX-6P-1-PIF6 (14-37)	This paper	N/A
pGEX-6P-1-PIF6 (15-64)	This paper	N/A
pGEX-6P-1-PIF6-100^{E19A}	This paper	N/A
pGEX-6P-1-PIF6-100^{L20S}	This paper	N/A
pGEX-6P-1-PIF6-100^{F22A}	This paper	N/A
pGEX-6P-1-PIF6-100^{G25A}	This paper	N/A
pGEX-6P-1-PIF6-100^{I27S}	This paper	N/A
pGEX-6P-1-PIF6-100^{Q32A}	This paper	N/A
pGEX-6P-1-PIF1-FL	This paper	N/A

(Continued on next page)

Continued

REAGENT or RESOURCE	SOURCE	IDENTIFIER
pGEX-6P-1-PIF3-FL	This paper	N/A
pGEX-6P-1-PIF6-100-Strep	This paper	N/A
pCAMBIA1302-phyB-GFP	This paper	N/A
pCAMBIA1302-phyB^{Y83W}-GFP	This paper	N/A
pCAMBIA1302-phyB^{I101E}-GFP	This paper	N/A
pCAMBIA1302-phyB$^{Q109A/R110A}$-GFP	This paper	N/A
pCAMBIA1302-phyB^{L226Y}-GFP	This paper	N/A
pCAMBIA1302-phyB^{F314A}-GFP	This paper	N/A
pCAMBIA1302-phyB^{S584E}-GFP	This paper	N/A
pCAMBIA1302-phyB^{I228E}-GFP	This paper	N/A
pCAMBIA1302-phyB^{F420E}-GFP	This paper	N/A
pUC19-phyB^{Y276H}-HA	This paper	N/A
pUC19-phyB^{Y276H}-FLAG	This paper	N/A
pUC19-Myc-PIF1	This paper	N/A
pUC19-Myc-PIF3	This paper	N/A
pRSFDuet-1-HO1+Hy2	This paper	N/A
Software and algorithms		
CryoSPARC v4.1.2	Punjani et al.[80]	https://cryosparc.com/
RELION v3.3.1	Zivanov et al.[81]	https://www3.mrc-lmb.cam.ac.uk/relion
AlphaFold2	Jumper et al.[77]	alphafold.ebi.ac.uk/
PyMOL	Version 1.8 Schrödinger	https://pymol.org/2/
UCSF Chimera X v1.17.1	Meng et al.[82]	https://www.cgl.ucsf.edu/chimerax/
COOT v0.9.8.7	Emsley and Cowtan[83]	www2.mrc-lmb.cam.ac.uk//personal/pemsley/coot
PHENIX v1.20.1	Adams et al.[84]	https://phenix-online.org/
Origin 2022	OriginLab	https://www.originlab.com
GraphPad Prism 10	GraphPad	https://www.graphpad.com
Image J	NIH	https://imagej.nih.gov/ij/
ESPript v3.0	Robert and Gouet[85]	https://espript.ibcp.fr//ESPript/

EXPERIMENTAL MODEL AND SUBJECT DETAILS

Bacterial strains

Bacterial strain *Escherichia coli* BL21 (DE3) was used for expression of PIF and phytochromobilin (PΦB) in this work. Bacteria were cultured in LB medium (Oxoid) at 37°C until OD$_{600}$ reached 0.6–1.0, protein expression was induced by addition of 0.8 mM Isopropyl-β-D-thiogalactoside (IPTG, Sigma-Aldrich) at 16°C for 10–12 h with 170 rpm in shaking incubator (ZQZY-CF8W, Zhi Chu).

Insect cell lines

Insect cell line *Spodoptera frugiperda* (Sf21) was used for expression of apo-phyB in this work. Cells were cultured in Sf-900 II SFM medium (Gibco) at 28°C with 120 rpm in shaking incubator (ZQZY-CF8W, Zhi Chu). Baculovirus infected cells were cultured at 28°C with 120 rpm for 48 h.

Plant materials and growth conditions

The *Arabidopsis thaliana* (*Arabidopsis*) mutant *phyB-9* was used in this study. To complement the *phyB-9* mutant plants with *PHYB* variants, the full-length genomic DNA fragment containing the promoter and coding sequence of phyB was cloned into pCAM-BIA1302 vector to generate the *pPHYB:phyB-GFP* construct. The *pPHYB:phyB-GFP* constructs carrying *PHYB* mutants were generated by site-directed mutagenesis(I-5™ 2×High-Fidelity Master Mix). All constructs were transformed into *phyB-9* mutant plants by the floral-dip method of *Agrobacterium tumefaciens* (GV3101) transformation. Homozygous transgenic lines were identified by sequencing, western blot, subcellular fluorescence imaging, and phenotypes.

Seeds were sterilized sequentially by 75% ethanol and 1% NaClO, and then plated on 1/2 MS medium (2.2 g/L MS salts, 5 g/L sucrose, and 7 g/L agar, pH 5.8). The transgenic seeds were selected on 1/2 MS medium supplemented with 25 μg/ml Hygromycin B.

The plated seeds were imbibed in the dark at 4°C for 3 days to induce vernalization, and were then exposed to white-light for 6 h of to induce germination. The *Arabidopsis* seedlings were grown in a growth room at 23°C and 70% relative humidity under a 16 h/8 h light/dark photoperiod. For red light treatment, 60 μmol·m^{-2}·s^{-1} red light was supplied for the *Arabidopsis* seedlings, unless otherwise specified.

METHOD DETAILS

Recombinant protein expression and purification

For purification of apo-phyB proteins, the construct of full length phyB (residues 1-1172, generated from the *Arabidopsis* cDNA library by a standard PCR-based cloning strategy, cloned into pFastBac-1 vector with a modified N-terminal 6×His-SUMO tag, and verified by sequencing) was expressed in Sf21 insect cells (Invitrogen) at 28°C. After recombinant baculovirus infection for 48 h, the cells were harvested by centrifugation. For biosynthesis of PΦB molecules, the construct of pRSFDuet-1-HO1+Hy2 (HO1 (residues 1-240) and Hy2 (residues 46-329) were codon-optimized in GENEWIZ, Inc., cloned into pRSFDuet-1, and confirmed by sequencing) was transferred into *E. coli* BL21 (DE3) in LB medium containing 60 μg/mL kanamycin. After the culture was cooled down to 16°C, 0.8 mM Isopropyl-β-D-thiogalactoside (IPTG, Sigma-Aldrich) and 100 μM 5-aminolevulinic acid (5-ALA, Sigma-Aldrich) were supplemented to induce PΦB biosynthesis for 10 h with 170 rpm in darkness. The cells were harvested by centrifugation in darkness or dim green-light.

For recombinant of holo-phyB proteins, pellets of cells expressing apo-phyB and PΦB were resuspended and mixed using lysis buffer (25 mM Tris-HCl (pH 8.0), 150 mM NaCl, 5% (v/v) glycerol and 20 mM imidazole) and lysed by sonication on ice in darkness or dim green-light. The lysate was cleared by centrifugation at 4°C, 13000 rpm for 1 h, and the supernatant was loaded onto columns containing Ni^{2+} resin for protein purification. The N-terminal 6×His-SUMO tag was removed using PreScission protease after 8 h digestion on the column, and the phyB proteins were further purified through ion-exchange column (RESOURCE Q6, Cytiva). The truncated (phyB-908, phyB^{Y276H}-908) or site-directed mutants of phyB were expressed and purified following the same procedure, while phyB (90-621) was purified from *E. coli* BL21 (DE3).

For protein purification of PIF segments, the constructs of GST-tagged PIF1-100, PIF3-100, PIF4-100, PIF4 (residues 1-43), PIF6-100, PIF6 (residues 1-37), and PIF7-100 (amplified from the *Arabidopsis* cDNA library by a standard PCR-based cloning strategy, cloned into pGEX-6P-1, and confirmed by sequencing) were expressed in *E. coli* BL21 (DE3) as described above. The supernatant containing proteins of GST-tagged PIF segments after sonication and centrifugation was loaded onto columns containing GS4B resins for purification. For the reconstitution of phyB-Pfr-PIF6, phyB^{Y276H}-908-PIF6, and phyB-908-PIF6 complexes, the N-terminal GST tag was removed using PreScission protease after 8 h digestion on the column. For the pull-down or phyB dark reversion assays, the proteins of GST-tagged PIF segments were eluted from columns by elution buffer (25 mM Tris-HCl (pH 8.0), 150 mM NaCl, 5% (v/v) glycerol and 20 mM reduced glutathione). All these PIF proteins were further purified using gel filtration. The strep tagged PIF3-100 and PIF6-100 were expressed and purified following the same procedures.

Reconstitution of the phyB-PIF6 complexes

The purified holo-phyB was exposed to red light (660 nm, a fluence rate of 219.6 μmol·m^{-2}·s^{-1}) at 4°C for 1 h, and then the phyB proteins were incubated with an excess amount of PIF6-100 proteins by a molar ratio about 1:10 for 1 h on ice in red light (660 nm, 219.6 μmol·m^{-2}·s^{-1}). The phyB-Pfr-PIF6 complex was further purified using gel filtration under red light. The phyB-908-PIF6 complex was reconstituted following the same procedure. For the reconstitution of phyB^{Y276H}-908-PIF6 complex, the purified phyB^{Y276H}-908 proteins were incubated with PIF6-100 proteins by a molar ratio about 1:1.5 on ice in darkness, and the phyB^{Y276H}-908-PIF6 complex was further purified using gel filtration under dim green-light.

Gel filtration assays

The phyB-Pr, phyB-Pfr and phyB-Pfr-PIF6 complex were purified using gel filtration (Superose 6 Increase 10/300 GL, Cytiva) with the buffer containing 25 mM Tris-HCl (pH 8.0), 150 mM NaCl, 2% glycerol and 3 mM DTT either in darkness or under red light (660 nm, 219.6 μmol·m^{-2}·s^{-1}). These assays were performed with a flow rate of 0.5 mL/min and an injection volume of 2 mL. Ovalbumin (44 kDa), aldolase (158 kDa), ferritin (440 kDa) and thyroglobulin (669 kDa) were used as standard protein markers. The phyB-908-Pr, phyB-908-Pfr and phyB-908-PIF6 complexes were purified by gel filtration (Superdex 200 Increase 10/300 GL, Cytiva) with an injection volume of 100 μL following the same procedure, while phyB^{Y276H}-908 and phyB^{Y276H}-908-PIF6 complex were purified by gel filtration (Superdex 200 Increase 10/300 GL, Cytiva) with an injection volume of 2 mL in dim green-light. All the protein samples were examined by SDS-PAGE followed by Coomassie brilliant blue staining or zinc-induced fluorescence. The PIF6-100, PIF3-100-strep, and PIF6-100-strep were purified by gel filtration (Superdex 75 Increase 10/300 GL, Cytiva) following the same procedure. The GST-tagged PIF1-100, PIF3-100, PIF4-100, PIF4 (1-43), PIF6-100, PIF6 (1-37), and PIF7-100 were purified through gel filtration (Superdex 200 Increase 10/300 GL, Cytiva).

Cryo-EM sample preparation and data collection

For cryo-EM sample analyses of phyB-Pfr-PIF6 and phyB^{Y276H}-908-PIF6, a 3.5 μL volume aliquot of 1.5 mg/mL phyB-Pfr-PIF6 or phyB^{Y276H}-908-PIF6 sample was applied to a glow-discharged grids (Au R1.2/1.3 grid (C-flat), 300-mesh). Grids were blotted for

3–4.5 s with filter paper and plunged into liquid ethane using an FEI Mark IV Vitrobot (Thermo Fisher Scientific) operated at 4 °C and 100% humidity. Then, grids were stored in liquid nitrogen for the further research. Cryo-EM images were collected on a Titan Krios electron microscope operated at 300 kV and a Gatan K3 Summit direct electron detection camera (Gatan) using EPU software. Images stacks were recorded in super-resolution mode at a nominal magnification of 105,000×, corresponding to a physical pixel size of 0.85 Å per pixel, with a defocus range between -1 μm and -2 μm. The dose rate was 15 electron per pixel per second. Exposures of 2.41 s were dose-fractionated into 40 subframes, leading to a total dose of 50 electrons per Å^2.

Cryo-EM data processing

For phyB-Pfr-PIF6 complex, 7,310 movies were collected. The raw super-resolution dose-fractionated images stacks were 2 × Fourier binned, aligned, dose-weighted and summed using Patch Motion Correction in cryoSPARC, resulting in summed micrographs in a pixel size of 0.85 Å per pixel. Contrast transfer function (CTF) parameters were estimated using Patch CTF Estimation in cryoSPARC. After excluding the micrographs with bad Thon rings, 5,489 micrographs were selected for subsequent processing. Blob picker was performed on a random subset of 1000 micrographs, and around 2,800,000 particles were selected for several rounds of 2D classification to generate a template for the further template picking. 345,630 particles with good quality were used to perform ab initio 3D reconstruction in cryoSPARC to generate 3D volumes used for further reference-based 3D classification in RELION. These selected particles were also used to perform Topaz training, and the trained model was further applied to all 5,489 micrographs, and 3,360,071 particles were selected and extracted with pixel size of 2.55 Å per pixel. After a round of 2D classification in cryo-SPARC, 2,676,259 particles were selected and performed three rounds of 3D reference-based classification in RELION. A total of 325,483 particles were re-extracted with pixel size of 0.85 Å per pixel and then used for homogeneous refinement and further local refinement in cryoSPARC with initial volume generated from 3D classification. Finally, a high-quality cryo-EM map was obtained, with an estimated resolution of 3.10 Å determined by gold-standard Fourier shell correlation (FSC) 0.143, for the subsequent structural model building. Parameters for data processing and 3D reconstruction are summarized in Data S1; Table S1.

For phyB^{Y276H}-908-PIF6 complex, 15,142 movies were collected. Motion correction and CTF estimation were performed in cryoSPARC as described above. After excluding the micrographs with bad Thon rings, 14,636 micrographs were selected for subsequent processing. Template picker was performed on all these micrographs, and around 16,839,000 particles were selected and extracted with pixel size of 1.70 Å per pixel for several rounds of 2D classification. 537,616 particles were used to perform ab initio 3D reconstruction in cryoSPARC to generate 3D volumes and subsequent heterogeneous refinement. A total of 36,6884 particles were re-extracted with pixel size of 0.85 Å per pixel and then used for homogeneous refinement and further local refinement with the original volume in cryoSPARC. Finally, a high-quality cryo-EM map was obtained, with an estimated resolution of 3.19 Å determined by gold-standard Fourier shell correlation (FSC) 0.143, for the subsequent structural model building. Parameters for data processing and 3D reconstruction are summarized in Data S1; Table S1.

Model building and refinement

For phyB-Pfr-PIF6 complex, the predicted 3D model of phyB monomer and PIF6 from Alphafold2 was used as the initial template. The models of phyB-Pfr and PIF6-100 were fitted into the EM density map using UCSF ChimeraX, followed by manual adjustment and rebuilding in COOT. PDB file of PΦB was separated from PDB-8ISJ. The model of phyB-Pfr-PIF6 complex was refined by real-space refinement (phenix.real_space_refine) in Phenix and manual adjustment in COOT. For phyB^{Y276H}-908-PIF6 complex, the model of phyB-Pfr-PIF6 was used as the initial template. The subsequent modeling building and refinement were performed following the same procedure. The structural model statistics are summarized in Tables S1 and S2.

in vitro Pull-down assays

For phyB-PIF interactions, an excess amount of phyB proteins was individually incubated with the GST-tagged PIF segments on the beads in red light (660 nm, 219.6 μmol·m^{-2}·s^{-1}) (or white-light for phyB^{Y276H}) at 4°C for 1 h. After washing with 5 mL lysis buffer (25 mM Tris-HCl (pH 8.0), 150 mM NaCl, 5% (v/v) glycerol) for four times, the GS4B beads were then analyzed by SDS-PAGE, zinc-induced fluorescence under UV-light, and Coomassie brilliant blue staining.

For the 2:1 stoichiometry between phyB and PIF-100, the equal amounts of GST- and strep-tagged PIF6-100 (or PIF3-100) proteins were mixed with an excess amount of phyB-908 proteins in red light (660 nm, 219.6 μmol·m^{-2}·s^{-1}) (or the phyB^{Y276H}-908 proteins in white light) at 4°C for 1 h. Then one-half of the mixture was incubated with GS4B beads, and the other half was incubated with strep beads. After incubation for 30 min, the beads were washed with 5 mL washing buffer (25 mM Tris-HCl (pH 8.0) and 150 mM NaCl) for four times. Proteins bound to beads were separated on a 15% SDS-PAGE gel and detected by zinc-induced fluorescence under UV-light, Coomassie brilliant blue staining, or anti-Strep immunoblot.

Co-Immunoprecipitation (CoIP) assays

For detection of the molar ratio between phyB and full-length PIFs *in vitro*, the equal amounts of HA-tagged and FLAG-tagged phyB^{Y276H} were co-incubated with or without an excess amount of GST-tagged full-length PIF1 or PIF3 synthesized by the *in vitro* transcription-translation system (TNT® SP6 High-yield Wheat Germ Protein Expression System, Promega) as described previously in white-light at 4°C for 1 h.[20,86] Then one-half of the mixture was incubated with anti-HA beads (Smart-Lifesciences), and the other half was incubated with anti-FLAG beads (Smart-Lifesciences). After incubation for 1 h, the beads were washed with 5 mL washing

buffer (25 mM Tris-HCl (pH 8.0) and 150 mM NaCl) for four times. Proteins precipitated by the beads were separated on a 10% SDS-PAGE gel and detected by anti-HA, anti-GST, or anti-FLAG immunoblot.

For Co-IP assays of the protoplast-expressed full-length version of phyB and PIFs, protoplasts from *Arabidopsis* (Col-0) were individually transfected with the phyB^{Y276H}-HA, phyB^{Y276H}-FLAG, Myc-PIF1, and Myc-PIF3 constructs. These proteins were expressed overnight in darkness. Equal volume of protoplasts expressing phyB^{Y276H}-HA and phyB^{Y276H}-FLAG were mixed with an excess amount of protoplasts expressing Myc-PIF1 or Myc-PIF3. The total proteins were extracted with protein extraction buffer (50 mM HEPES pH 7.5, 150 mM KCl, 1 mM EDTA, 0.5% Trition-X100, 1 mM DTT, protease inhibitor cocktail) in white-light. One half of the total proteins was incubated with 50 μL anti-FLAG beads (Smart-Lifesciences), while the residual was incubated with 50 μL anti-HA beads (Smart-Lifesciences). After incubation for 40 min at 4°C in white-light, the beads were washed six times with washing buffer (50 mM HEPES pH 7.5, 150 mM KCl, 1 mM EDTA, 0.5% Trition-X 100, 1 mM DTT). Proteins precipitated by the beads were separated on a 10% SDS-PAGE gel and detected by anti-HA, anti-Myc, and anti-FLAG immunoblot.

Immunoblot assays

Five-day-old *Arabidopsis* seedlings grown under continuous red light were ground into powder in liquid nitrogen. The powder was then homogenized with protein extraction buffer (50 mM Tris-HCl (pH 8.0), 150 mM NaCl, 5% SDS). After centrifugation at 12000 rpm for 5 min, the supernatant containing the total protein mixture was collected. Proteins extracted from seedlings were separated using 8–12% SDS-PAGE. Following electrophoresis, the proteins were transferred to a polyvinylidene difluoride membrane (PVDF, Roche) at 100 V for 45 min at 4°C. To block non-specific binding, the membrane was treated with 5% skimmed blocking solution (5% (w/v) skim milk in TBS with 0.5% (w/v) Tween 20), and incubation was carried out by gentle agitation for 1 h at room temperature or overnight at 4°C. The anti-GFP (EASYBIO, diluted 1:2000) and anti-Actin (EASYBIO, diluted 1:2000) antibodies were used for immunoblot analyses. The immunoblot assays for protein detection in the aforementioned pull-down or Co-IP assays by anti-Strep (Sangon Biotech, diluted 1:2000), anti-HA (Abmart, diluted 1:2000), anti-FLAG (Sigma-Aldrich, diluted 1:2000), anti-GST (Abcam, diluted 1:2000), and anti-Myc (Sigma-Aldrich, diluted 1:2000) antibodies were performed following the same procedure.

Subcellular fluorescence imaging

The transgenic *Arabidopsis* seedlings expressing phyB-GFP were grown in the dark for 5 days and were then exposed to red light for 8 h. The hypocotyl cells were observed using a confocal laser scanning microscope (Nikon A1 HD25+SIM) with GFP fluorescence excited at 488 nm.

UV-vis absorption spectroscopy and kinetics of dark reversion

UV-vis absorption spectra of phyB proteins were measured by Cary60 spectrophotometer (Agilent) equipped with temperature-controlled cuvettes PCB-1500 at 22°C using sub-micro cell quartz (10 mm 50 μL, Agilent). To maintain the consistency of spectral measurements, the buffer for cryo-EM sample preparation of phyB-Pfr-PIF was chosen for assays. The phyB samples were treated with far-red light (740 nm, 50.4 μmol·m^{-2}·s^{-1}) irradiation for 30 min, followed by further dark treatment for 1 h, before the spectral measurements of Pr. For the following spectral measurement of Pfr, the same samples were used after the saturating irradiation with red light (630 nm, 340.1 μmol·m^{-2}·s^{-1}). The absorbance of continuous wavelength ranging from 200-900 nm was collected for all these measurements. The scan rate was 4800 nm/min. The difference spectra were generated by a subtraction of the Pfr spectrum from the Pr spectrum.

For the measurements of Pfr-to-Pr dark reversion, the phyB samples (phyB alone or mixed with GST-tagged PIF in a molar ratio about 1:10) were treated with far-red light (740 nm, 50.4 μmol·m^{-2}·s^{-1}) until they reached a steady state. We recorded the absorbance at 660 nm and 725 nm in this state, which were labeled as Pr$_{max}$ and Pfr$_{min}$, respectively. Then the phyB samples were exposed to red light (630 nm, 340.1 μmol·m^{-2}·s^{-1}) until they reached another steady state. The absorbance at 660 nm and 725 nm at this state were labeled as Pr$_{min}$ and Pfr$_{max}$, respectively. Thus, the difference between Pfr$_{max}$ and Pfr$_{min}$ was defined as 100% of phyB-Pfr. Similarly, the difference between Pr$_{max}$ and Pr$_{min}$ was defined as 0% of phyB-Pr. Then the absorbance at 725 nm or 660 nm was recorded with appropriate time intervals to evaluate dark reversion of phyB samples at 22°C in darkness. Simulated kinetic profiles for dark reversion were calculated by exponential decay fits of the normalized data points as described previously.[54] All spectroscopy data were collected using Cary WinUV software, and all the data were processed and fit using GraphPad Prism10.

QUANTIFICATION AND STATISTICAL ANALYSIS

All spectroscopic data were recorded using Cary 60 spectrophotometer (Agilent) and presented as means calculated in three biological replicates. Hypocotyl length and cotyledon angle were measured using ImageJ software (https://imagej.nih.gov/ij/), with a minimum of 20 samples measured for each genotype. The collected data were analyzed using Origin 2022 (https://www.originlab.com/2022) or GraphPad Prism 10 (https://www.graphpad.com). Statistical analyses and graph constructions were performed using one-way ANOVA, followed by Tukey's post-hoc test ($P < 0.05$). Further details can be found in the figure legends.

Supplemental figures

(legend on next page)

Figure S1. Characterization of phyB proteins, pull-down assays for phyB-PIF interactions, and topology of phyB-Pfr or phyB^Y276H, related to Figure 1

(A) Left: UV-vis absorbance spectra of phyB-FL in darkness (D) and after saturating irradiation with red light (R). The spectral change ratio (SCR) values are indicated in parentheses. Right: a cyan color of phyB in Pr state and a light green color after red light saturation.

(B) Left: UV-vis absorbance spectra of phyB^Y276H-908 in darkness (D) and after irradiation with red light (R). Right: a cyan color of phyB^Y276H-908 in Pr state or after red light irradiation.

(C) Pull-down assays for phyB-PIF interactions in dim green light or red light. The pull-down samples were analyzed by SDS-PAGE, followed by Coomassie brilliant blue staining (left) or zinc-induced fluorescence assay (right).

(D) Zinc-induced fluorescence assays for phyB-Pfr-PIF6 (top) and phyB^Y276H-908-PIF6 (bottom).

(E) Topological schematic of phyB-Pfr or phyB^Y276H generated from the structure models of the phyB-Pfr-PIF6 or phyB^Y276H-908-PIF6 complexes. The secondary structural elements of the N-terminal PSM containing NTE, nPAS, GAF and its knot lasso (KL) as well as PHY and its tongue are shown. The C-terminal hinge region (PAS1-PAS2) and HKRD are flexible in the cryo-EM map.

A phyB-Pfr *vs* Pr (protomer a)   phyB-Pfr *vs* Pr (protomer b)

B phyB-Pr *vs* phyB-Pfr (protomer a)   phyB-Pr *vs* phyB-Pfr (protomer b)

C

D phyB-Pfr(b, colored)   DrBphP-Pfr

E phyB-Pfr *vs* DrBphP-Pfr

F phyB-Pfr *vs* DrBphP-Pfr

G

H phyB-Pfr(colored)   phyB^Y276H-908

I phyB-Pr *vs* phyB^Y276H-908 *vs* phyB-Pfr (protomer a)

J phyB-Pr *vs* phyB^Y276H-908 *vs* phyB-Pfr (protomer b)

K
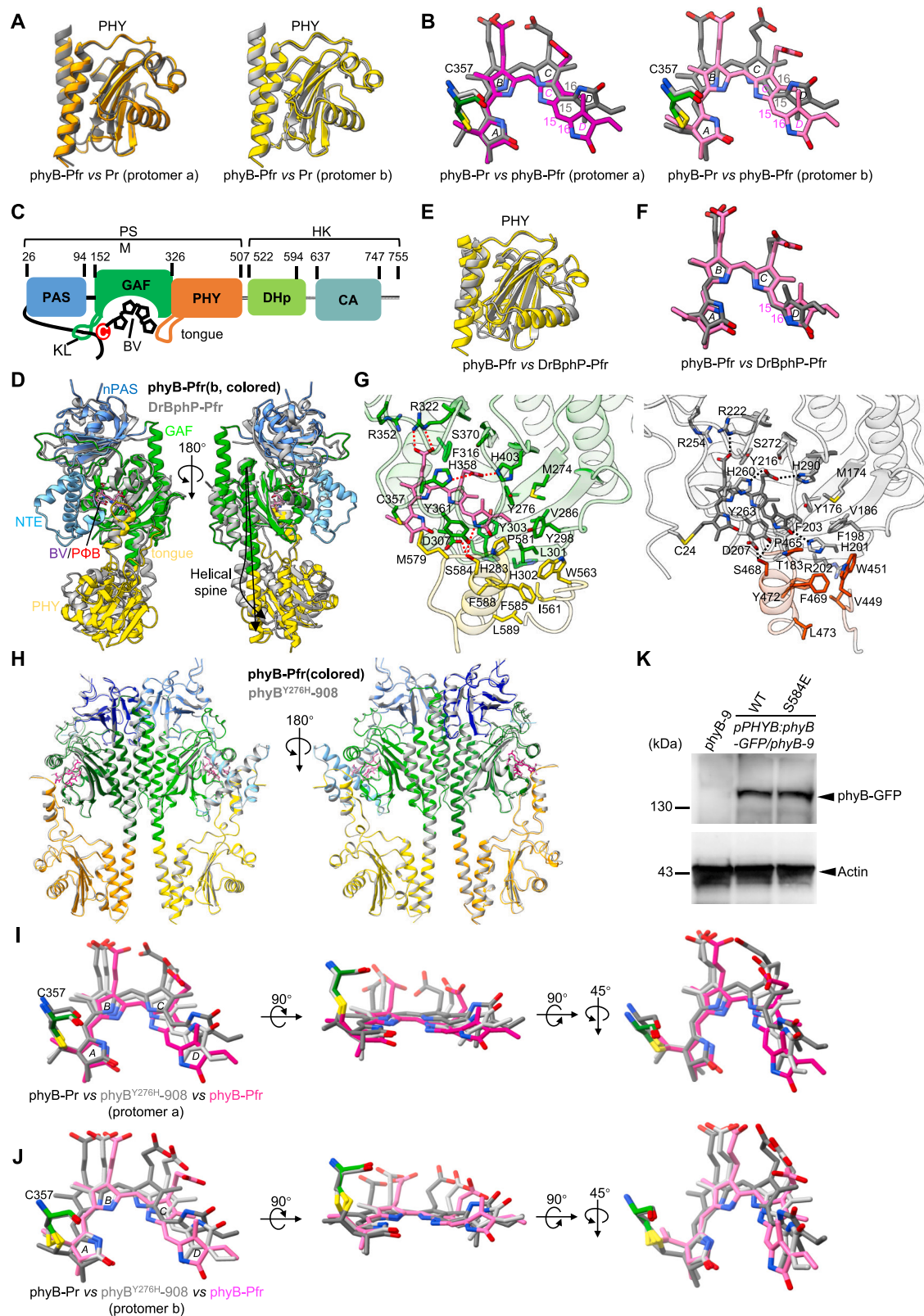
(legend on next page)

Figure S2. Mechanisms underlying the configuration switch of PΦB or BV chromophore and the conformational transition of the PHY tongue in phyB or DrBphP, related to Figure 2

(A) Alignment of the PHY domain between phyB-Pfr (left: protomer-a, orange; right: protomer-b, yellow) and phyB-Pr (gray, PDB: 7RZW).

(B) Alignment of PΦB structures of phyB-Pfr (carbon atoms in magenta) and phyB-Pr (carbon atoms in gray; PDB: 7RZW) from protomer-a (left) or protomer-b (right).

(C) Color-coded domain architecture of full-length DrBphP. BV, biliverdin IXα.

(D) Structural alignment of phyB-Pfr (color-coded) and DrBphP-Pfr (gray, PDB: 8AVX) in two orientations. Black arrows indicate the orientation of the helical spine.

(E) Structural comparison of the PHY domain between phyB-Pfr (yellow) and DrBphP-Pfr (gray).

(F) Alignment of PΦB from phyB-Pfr (carbon atoms in magenta) and BV from DrBphP-Pfr (carbon atoms in gray).

(G) Details of the chromophore-binding pocket of phyB-Pfr (left) and DrBphP-Pfr (right). PΦB (magenta) or BV (gray) and their contacting residues in the GAF domain (phyB: green; DrBphP: gray) and PHY domain (phyB: yellow; DrBphP: gray) are shown in sticks. Hydrogen bonds are indicated by red (phyB) or black (DrBphP) dashed lines.

(H) Alignment of phyB-Pfr (color-coded) and phyB^{Y276H}-908 (gray) in two orientations.

(I and J) Alignment of PΦB structures of phyB-Pr (carbon atoms shown in dark gray, PDB: 7RZW), phyB^{Y276H}-908 (carbon atoms shown in light gray), and phyB-Pfr (carbon atoms in magenta) from protomer-a (I) or protomer-b (J) in three orientations.

(K) The GFP-tagged phyB^{S584E} proteins expressed in 5-day-old transgenic seedlings grown under continuous red light (Rc) were detected by immunoblot assay.
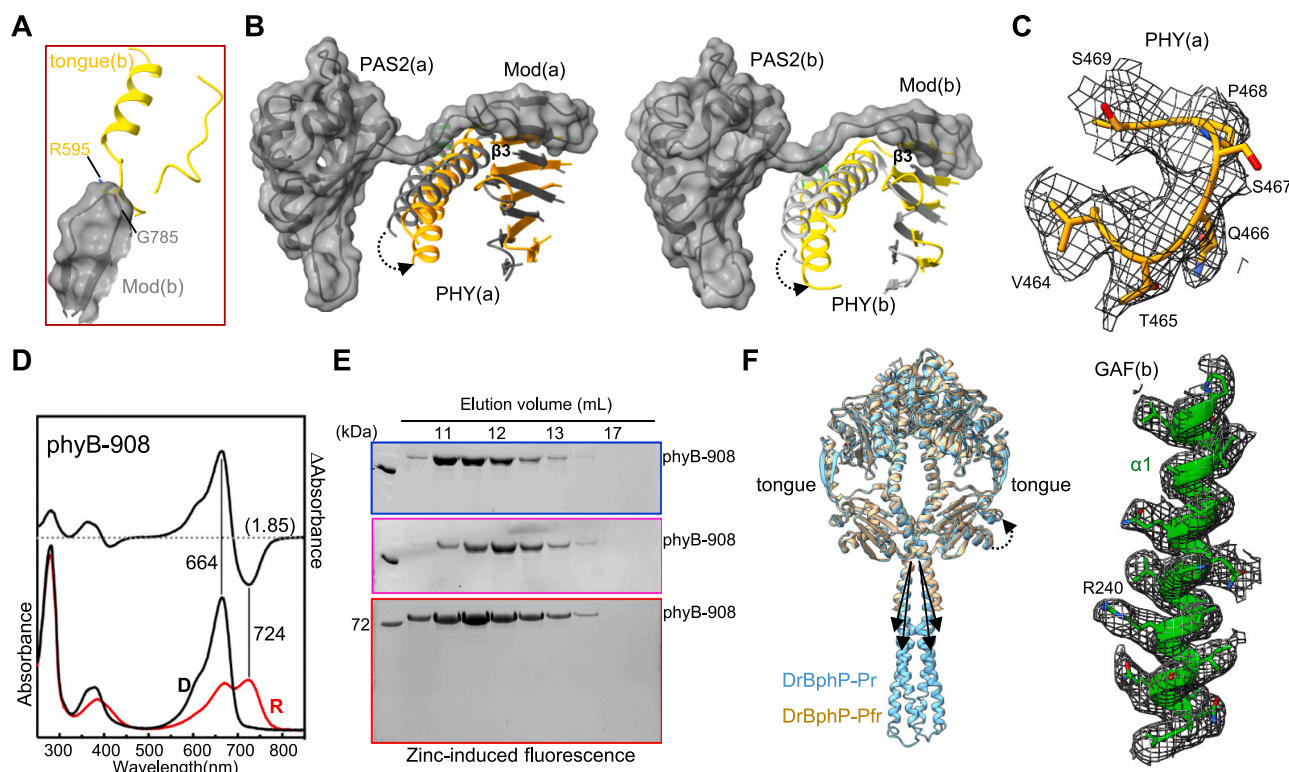
Figure S3. Transition of PHY tongue destructs the phyB-Pr dimer stabilized by the PAS2-HKRD module, related to Figure 3

(A) Details of clashes between α-helical PHY tongue (yellow) and Mod of PAS2 (gray) of protomer-b, indicated by red box in Figure 3B.

(B) Rotation of the PHY domain further abolishes contacts between PHY and PAS2, following the clash between the PHY tongue and Mod of PAS2. The PHY domain of protomer-a (left) or protomer-b (right) of phyB-Pfr is shown in orange or yellow, respectively. The PHY domain of phyB-Pr is shown in gray. The PAS2 domain of phyB-Pr is shown in gray and surface. The dashed arrow indicates the rotation of PHY domain from Pr to Pfr state. The PHY-β3 shifts to the position where the Mod was originally located.

(C) Top: the cyro-EM densities (black mesh) well define the residues (in sticks) of PHY that clash with HKRD during photoactivation in phyB(a). Bottom: the cyro-EM densities (black mesh) well define the residues (in sticks) of GAF-α1 that clash with HKRD during photoactivation in phyB(b).

(D) UV-vis absorbance spectra of phyB-908 proteins in darkness (D) and after saturating irradiation with red light (630 nm, 340.1 μmol·m^{-2}·s^{-1}) (R). The spectral change ratio (SCR) values are indicated in parentheses.

(E) Zinc-induced fluorescence assays for light-induced destruction of phyB-908 dimer in Pr state.

(F) Structural comparison of DrBphP-Pfr (wheat, PDB: 8AVX) and DrBphP-Pr (cyan, PDB: 8AVW). The dashed arrow indicates the shift in the PHY domain. Black arrows indicate the orientations of the C-terminal HK domains.

A phyB-Pfr-PIF6-100(colored)
phyB[Y276H]-908-PIF6-100

B

C

D

PIF6

APB-β

β1 TT β2

PIF6	..............MMF LPTD YCCRLS......DQEYMELVFENGQILAKGQRSNVSL
PIF1	MHHFVPDFDTDDDYVNNHSSLNHLPRKSITTMGEDDDLMELLWQNGQVVVQNQRLHTKK
PIF3	....MPLFELFRLTKAKLESAQDRNPSPP.....VDEVVELVWENGQISTQSQSSRSRN
PIF4	......MEHQGWSFEENYSLSTNRRSIRP.....QDELVELLWRDGQVVLQSQTHREQT
PIF5	....MEQVFADWNFEDNFHMSTNKRSIRP.....EDELVELLWRDGQVVLQSQARREPS

APB-α

α1 TT

PIF6	HNQRTKSIMDLYEAEYNEDFMKSIIHGGGGAITNLGDTQVVPQSHVAAAHET..
PIF1	PSSSPPKLLPSMDPQQQPSSDQNLFIQEDEMTSWLHYPLR.............
PIF3	IPPPQANSSRAREIGNGSKTTMVDEIPMSVPSLMTGLSQDDDFVPWLNHH...
PIF4	QTQKQDHHEEALR..SSTFLEDQETVSWIQYPPDEDPFEPDFSSHFFSTMDPL
PIF5	.VQVQTHKQETLRKPNNIFLDNQETVQKPNYAALDDQ..ETVSWIQYPPDDVI

E

F

(legend on next page)

Figure S4. Mechanisms of PIF6-100 or PIF3-100 recognition by phyB-Pfr or phyB[Y276H], related to Figure 4

(A) Alignment of phyB-Pfr-PIF6 (color-coded) and phyB[Y276H]-908-PIF6 (gray) structures in two orientations. PIF6-100 binds to phyB-Pfr or phyB[Y276H] in a similar manner.

(B) Mutations of PIF3-APB-β affected phyB-PIF3 interaction *in vitro*, as assayed in Figure 4D. The full SDS-PAGE gels were visualized by Coomassie brilliant blue staining (left) and zinc-induced fluorescence (right).

(C) Mutations of PIF6-APB-β affected phyB[Y276H]-PIF6 interaction *in vitro*, as assayed in Figure 4D. The full SDS-PAGE gels were visualized by Coomassie brilliant blue staining (left) and zinc-induced fluorescence (right).

(D) The amino acid sequences of PIF1/3/4/5/6-100 were aligned based on the structure of PIF6-100 from phyB-PIF6 complex. The highly conserved APB-β motif and less conserved APB-α motif are indicated by red bars. The red solid circles indicate the residues involved in phyB-PIF6 interactions.

(E) The GFP-tagged phyB[I101E], phyB[Q109A/R110A], phyB[F314A], or phyB[L226Y] proteins expressed in 5-day-old transgenic seedlings grown under Rc were detected by immunoblot assay.

(F) Subcellular fluorescence observations indicate that the above mutant proteins are localized within the nucleus of transgenic seedlings but exhibit a diminished capacity to form photobodies. 5-day-old transgenic seedlings, grown in darkness and subsequently exposed to red light for 8 h. Red arrows indicate the nucleus. Scale bar: 50 μm (top) and 10 μm (bottom).
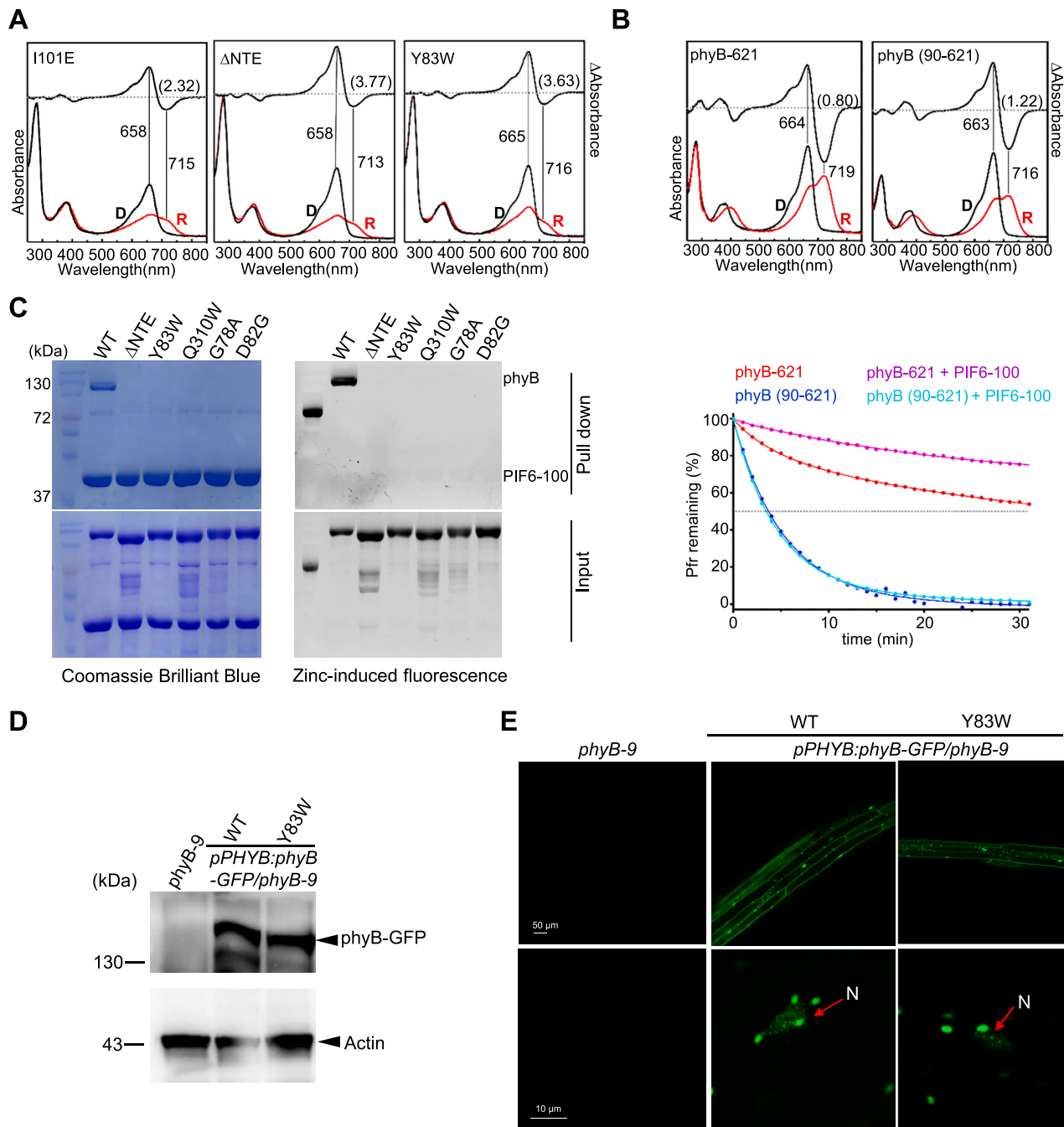
Figure S5. Mutations disrupting NTE-mediated intramolecular interactions affect dark reversion, PIF6 interaction, and signaling of phyB, related to Figure 5

(A) UV-vis absorbance spectra of the phyB-NTE mutant proteins in darkness (D), and after saturating irradiation with red light (630 nm, 340.1 μmol·m^{-2}·s^{-1}) (R). The spectral change ratio (SCR) values are indicated in parentheses.

(B) Top: UV-vis absorbance spectra of the phyB-621 (PSM) and phyB (90–621) in darkness (D) and after saturating irradiation with red light (R). Bottom: PIF6-100 effectively inhibited the Pfr-to-Pr dark reversion of phyB-PSM (phyB-621) but has no effect on phyB (90–621). The assays were performed as described for Figure 5C.

(C) The full SDS-PAGE gels were visualized by Coomassie brilliant blue staining (left) and zinc-induced fluorescence (right) for Figure 5E.

(D) The GFP-tagged phyB^{Y83W} proteins expressed in 5-day-old transgenic seedlings grown under Rc were detected by immunoblot assay.

(E) Subcellular fluorescence observations indicate that the GFP-tagged phyB^{Y83W} proteins expressed in transgenic seedlings are localized in the nucleus, but they form fewer photobodies compared with wild-type phyB. The assays were performed as described for Figure S4F.
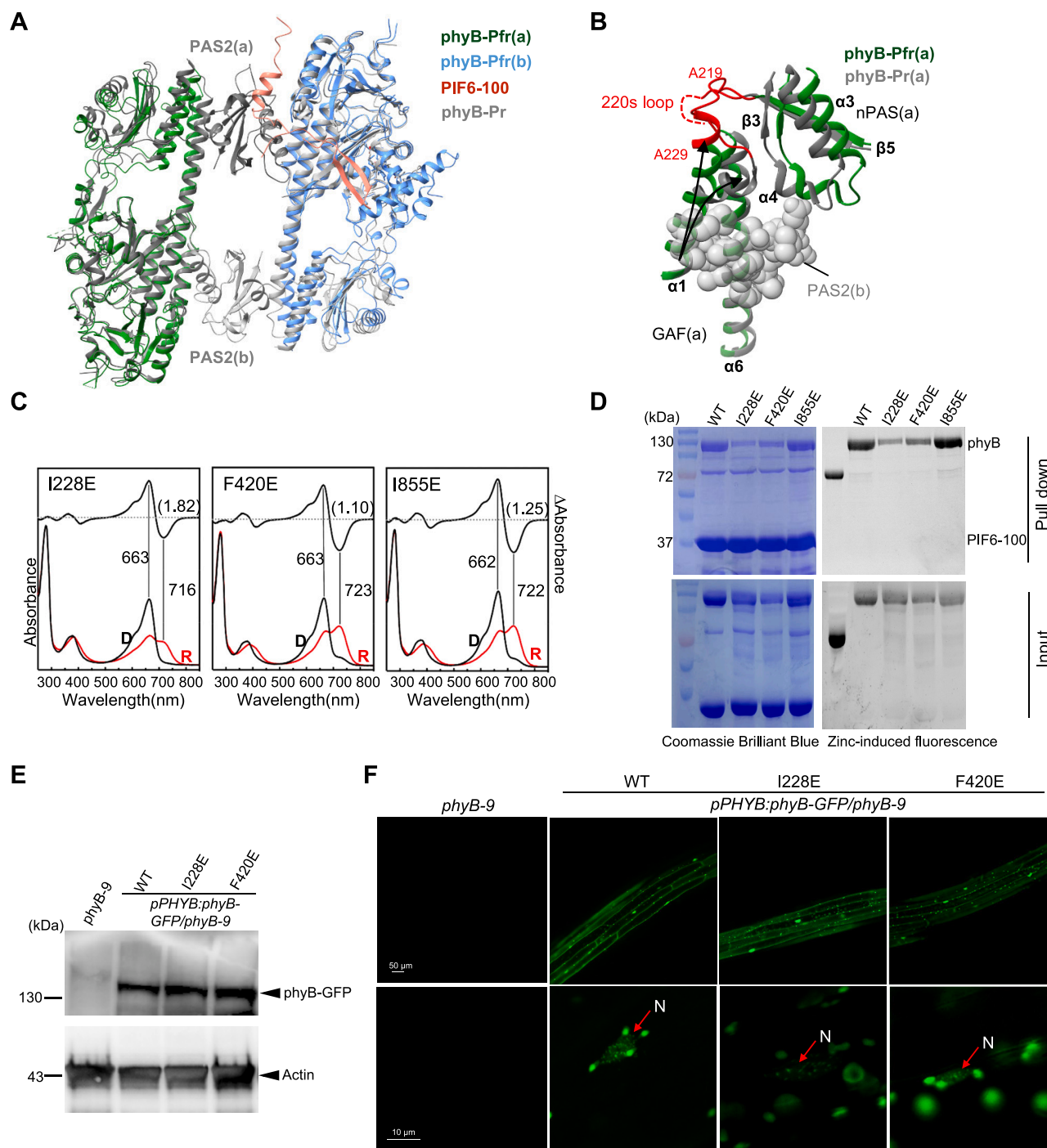
Figure S6. PIF6-APB-α induces and fits a head-to-head dimer of phyB-Pfr through the nPAS-GAF module, related to Figure 6

(A) Superposition of the PIF6-bound phyB-Pfr (blue) protomer and phyB-Pr dimer (gray, PDB: 7RZW). The other phyB-Pfr protomer (green) is aligned to the remaining protomer of phyB-Pr dimer. The PAS2 domain in phyB-Pr dimer is incompatible with PIF6-APB-α.

(B) Structural comparison of the nPAS-GAF module of phyB-Pfr (green) and phyB-Pr (gray, PDB: 7RZW). The PAS2 domain from the other phyB-Pr protomer, shown in sphere. The 220s loop colored in red. Arrows indicate the orientation of GAF-α1.

(C) UV-vis absorbance spectra of the phyB mutants, with impaired dimerization of phyB-Pfr or phyB-Pr, in darkness (D) and after saturating irradiation with red light (630 nm, 340.1 $\mu mol \cdot m^{-2} \cdot s^{-1}$) (R). The spectral change ratio (SCR) values are indicated in parentheses.

(D) The full SDS-PAGE gels were visualized by Coomassie brilliant blue staining (left) and zinc-induced fluorescence (right) for Figure 6F.

(legend continued on next page)

(E) The GFP-tagged phyB^{I228E} and phyB^{F420E} proteins expressed in 5-day-old transgenic seedlings grown under Rc were detected by immunoblot assay.
(F) Subcellular fluorescence observations indicate that these mutant proteins expressed in transgenic seedlings are localized in the nucleus, but the photobodies they formed are less stable than those of wild-type phyB. The assays were performed as described for Figure S4F.

A

nPAS
α4
phyB-Pfr *vs* Pr (protomer a)

nPAS
α4
phyB-Pfr *vs* Pr (protomer b)

nPAS
α4
phyB-Pfr (a) *vs* **phyB-Pfr (b)**

C

PIF6
phyB-Pfr(a)
phyB-Pfr(b)
phyB-PSM-Pr
protomer a   protomer b

B

-	+	-	+	-	+	-	-	-	-	-	-	GST-PIF1
-	-	-	-	-	-	-	+	-	+	-	+	GST-PIF3
+	+	+	+	+	+	+	+	+	+	+	+	phyBY276H-HA
+	+	+	+	+	+	+	+	+	+	+	+	phyBY276H-FLAG

Anti-HA
Anti-FLAG
Anti-Myc

Input   IP: HA   IP: FLAG   Input   IP: HA   IP: FLAG

D

nPAS(a)   APB-α   nPAS(b)
α3   α3
α1   α1
GAF(a)   GAF(b)
α6   α6

E

phyB-Pfr (a)
phyB-Pfr (b)
phyB-PSM-Pr
PIF6-APB-α

α1   α1   α1   α1
GAF(b)   GAF(a)   GAF(b)   GAF(a)

F **Sb.phyB-Pr (nPAS-GAF)**

nPAS(a)   nPAS(b)
GAF(a)   GAF(b)
protomer a   protomer b

90°

α3
α6   α1
α6
α1
α3

G

PIF1(a)
PIF1(b)
APB(a)   APB(b)
bHLH(a)   bHLH(b)

H

PIF3(a)
PIF3(b)
APB(a)   APB(b)
bHLH(b)   bHLH(a)

I

PIF6(a)
PIF6(b)
APB(a)   APB(b)
bHLH(b)   bHLH(a)

J

phyB-PSM dimer
APB(a)   APB(b)
bHLH(a) bHLH(b)
phyB-PSM dimer   phyB-PSM dimer
phyB:PIF = 4:2

phyB-PSM dimer
APB(a)   APB(b)
bHLH(a)   bHLH(b)
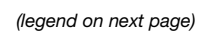phyB:PIF = 2:2

(legend on next page)

Figure S7. Mechanisms for the asymmetry in the phyB-Pfr dimer, the resulting 2:1 molar ratio of phyB-PIF6 interaction, and the predicted model of how this interaction mode affects the DNA-binding activity of PIF, related to Figure 7

(A) Alignment of the nPAS domain between phyB-Pfr (green or blue) and phyB-Pr (gray, PDB: 7RZW) from protomer-a (left) or protomer-b (middle). Alignment of the nPAS domain between protomer-a (green) and protomer-b (blue) in phyB-Pfr (right).

(B) *Arabidopsis* (Col-0) protoplasts individually expressing phyB^{Y276H}-HA and phyB^{Y276H}-FLAG were mixed and lysed, with or without an excess of protoplasts expressing Myc-PIF1 or Myc-PIF3. Total proteins were precipitated by anti-HA or anti-FLAG beads. After extensively washing, the precipitates were analyzed by the anti-HA, anti-FLAG, and anti-Myc immunoblot. The results clearly demonstrate enhanced detection of both phyB^{Y276H} variants in the presence of PIF1 or PIF3. Notably, the full-length PIF1 or PIF3 proteins display a smeared appearance in the immunoblots, indicative of hyperphosphorylation or proteolytic degradation of the protoplast-expressed PIF proteins.

(C) Structural comparison of PIF6-bound phyB-Pfr dimer (color-coded, in surface) and the PSM of phyB-Pr (gray, in cartoon; PDB: 4OUR).

(D) Details of the asymmetric dimerization interface mediated by the nPAS-GAF module in PIF6-bound phyB-Pfr (color-coded) and the PSM of phyB-Pr (gray), indicated by blue box in (C), shown in two orientations.

(E) The asymmetric GAF-α1 helices in the PIF6-bound phyB-Pfr dimer (left) and the PSM of phyB-Pr (right). PIF6-APB-α binds to GAF-α1 of phyB-Pfr protomer-a.

(F) Crystal structure of the nPAS-GAF segment of *Sorghum bicolor* phyB (Sb.phyB) reveals a symmetric dimerization mode (PDB: 6TC5).

(G–I) Structures of full-length homodimers of PIF1 (G), PIF3 (H), and PIF6 (I), as predicted by AlphaFold2, are depicted. The two protomers are distinguished by coloring in green and blue. The N-terminal APB motifs, which form β-hairpin structures, and the C-terminal α-helical bHLH domains are specifically indicated.

(J) Model on the 4:2 (2:1) or 2:2 (1:1) ratio of phyB and PIF. The predicted structures of PIF dimers (G–I) indicate that the two N-terminal PIF-APB motifs are spatially segregated on the opposite side of the C-terminal bHLH domains. A model depicting a 4:2 ratio of phyB to PIF, shown on the left, suggests that the binding of two phyB-PSM dimers to each PIF-APB motif may induce steric clashes with the PIF-bHLH dimer, consequently impairing its DNA-binding capability. Conversely, for a 2:2 ratio of phyB to PIF presented in the right, the PIF-APB motifs would require substantial conformational adjustments to accommodate a single phyB-PSM dimer. The cylinders indicate PIF-bHLH, rectangles indicate PIF-APB, and the irregular rectangles indicate the N-terminal PSM of phyB (phyB-PSM).
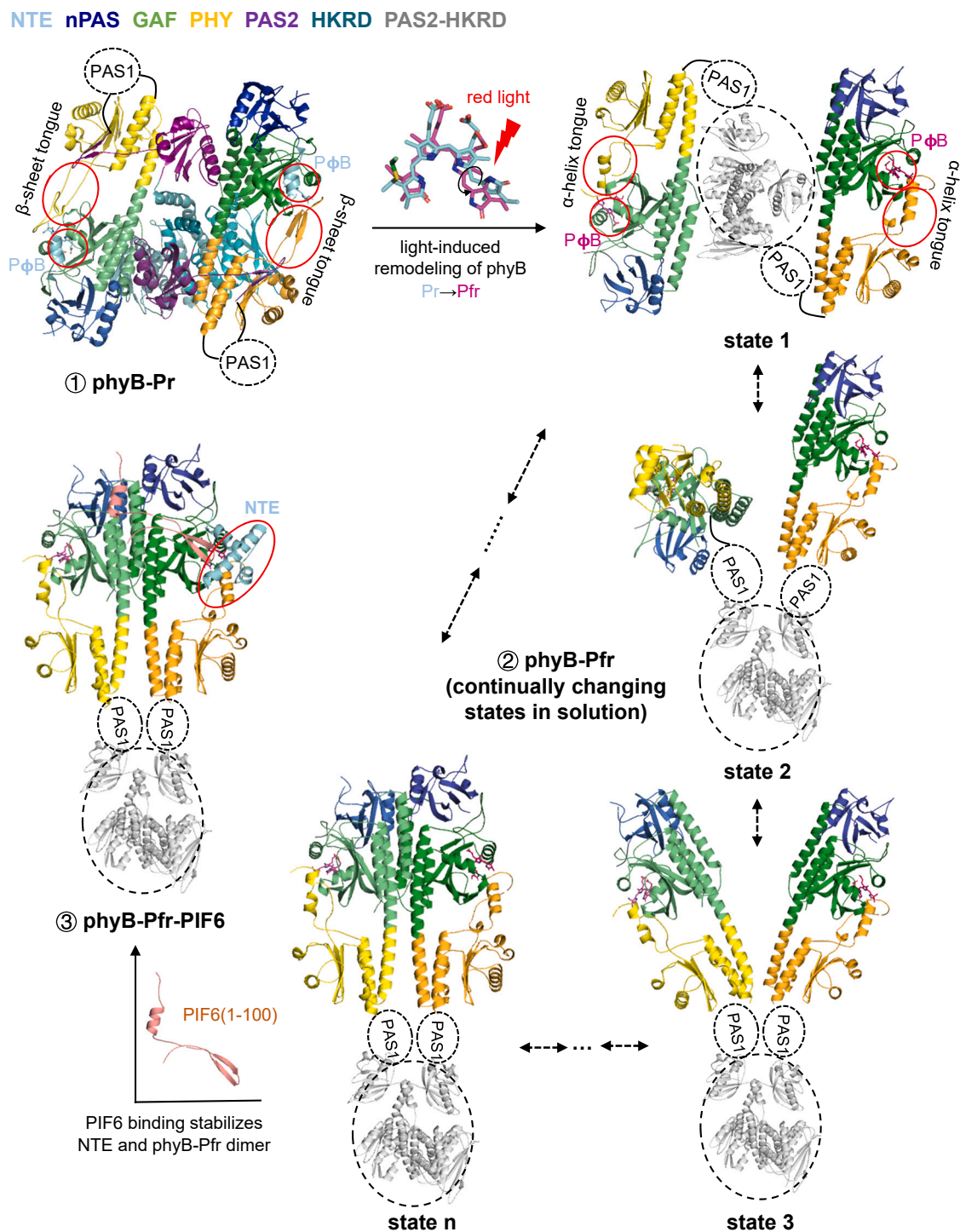
NTE nPAS GAF PHY PAS2 HKRD PAS2-HKRD

Figure S8. Model on light-activated phyB recognizing its PIF partner, related to Figure 7

In phyB-Pr (stage 1), the PAS2-HKRD module stabilizes a head-to-tail dimer. Upon red light irradiation, PΦB undergoes a configuration switch by flipping the D-ring, which facilitates a transition of the PHY tongue from a β-sheet in Pr to an α-helix in Pfr. This structural change leads to the dissociation of the C-terminal PAS2-HKRD module from the N-terminal PSMs. The resulting phyB-Pfr keeps dimeric by the C-terminal HKRD, while the free and monomeric N-terminal PSMs confer enhanced flexibility to phyB-Pfr in solution (stage 2). PIF6-100 binds to phyB-Pfr, thereby stabilizing the NTE and a head-to-head dimer of phyB-Pfr by the β-hairpin-forming APB-β and the α-helix-forming APB-α of PIF6-100, respectively (stage 3).